

Contents

| | |
|--|----|
| Table of Contents | i |
| List of Figures | i |
| List of Tables | iv |
| 1 Silicon Vacancy Centers in Diamond | 1 |
| 1.1 Diamond as a host lattice | 1 |
| 1.2 Classification of diamond | 2 |
| 1.2.1 Classification by impurities | 2 |
| 1.2.2 Classification by crystallinity | 3 |
| 1.3 Silicon-vacancy center | 4 |
| 1.3.1 Luminescence properties | 5 |
| 2 Coupling NDs | 11 |
| 2.1 Additional Experimental Methods | 12 |
| 2.1.1 Nanomanipulator | 12 |
| 2.1.2 Determination of The Position of Nanodiamonds | 13 |
| 2.1.3 The Pick-And-Place Process | 14 |
| 2.2 VCSELs | 15 |
| 2.2.1 Vertical-Cavity Surface Emitting Laser Structure | 16 |
| 2.2.2 SiV center in a Vertical-Cavity Surface Emitting Laser | 17 |
| 2.3 Antennas | 21 |
| 2.3.1 Plasmonic Antennas | 23 |
| 2.3.2 Structure of the Plasmonic Antennas | 25 |
| 2.3.3 SiV center in a Plasmonic Antenna | 26 |
| Bibliography | 29 |

List of Figures

| | | |
|-----|---|----|
| 1.1 | Face-centered cubic diamond lattice | 2 |
| 1.2 | Reduced light extraction efficiency of diamond due to refraction | 2 |
| 1.3 | Split-vacancy configuration for SiV centers in diamond | 5 |
| 1.4 | Band gap of SiV centers hosted in diamond | 6 |
| 1.5 | Huang-Rhys model of vibrational transitions | 8 |
| 1.6 | Flourescence spectra of SiV centers at room temperature | 9 |
| 1.7 | Flourescence spectra of SiV centers at low temperature | 10 |
| 2.1 | (a) Sketch of the pick-and-place process exploiting a nanomanipulator. (b) Image of the nanomanipulator mounted in the FIB. The arrows indicate the degrees of freedom of motion of the nanomanipulator. The custom made workbench is situated in the middle of the picture. On top of it, there is a 1 cm^2 substrate with coated nanodiamonds, the nanomanipulator tip pointing to the middle of it. Behind it, there is the target vertical-cavity surface emitting laser. Perpendicular to the workbench, the objective of the electron microscope can be seen. The pointier cone perpendicular to the image top image edge is the objective of the focussed ion beam. | 13 |
| 2.2 | (a) Overview of a field of cross markers. The field spans $0.5 \times 0.5\text{ mm}$ (b) White light scan of an area with a cross marker in all four corners. | 14 |
| 2.3 | | 15 |
| 2.4 | (a) Sketch of the VCSEL showing the different layers. ask how to cite (b) Image of the VCSEL. The circle with the black dots is the hole in the p-contact (diameter D_S , the smaller darker area in the middle is the laser output area (diameter D_A) | 16 |
| 2.5 | (a) Emission spectrum of the used VCSEL at two different currents. (b) Optical output power and voltage of the same VCSEL in dependence of input current. [] | 16 |
| 2.6 | (a) SEM image of an array of VCSELs. The three wires are the anodes, which are connected to the top layer (p-contact) of the VCSEL. Therefore, three of the VCSEL structures can be operated. (b) Detail SEM image of the top of the exploited VCSEL Bm4. The circular middle part is the hole in the p-contact through which the top DBR is visible. The active diameter is smaller than that and not visible in the SEM. | 17 |

| | | |
|------|---|----|
| 2.7 | (a) Scan of the VCSEL Bm4 with coupled nanodiamond under excitation with the laser from the confocal setup. The big visible ring is the edge of the circular hole in the p-contact. The bright spot in the upper left corner corresponds to the transferred nanodiamond containing an SiV center. (b) Scan of the VCSEL Bm2 without nanodiamond under excitation with the laser from the confocal setup. The circular hole in the p-contact exhibits a constant countrate. | 18 |
| 2.8 | (a) Spectrum of the preselected diamond for transfer onto VCSEL Bm4 before pick-and-place. The strong line denoted A exhibits a center wavelength of 746.0 nm and a linewidth of 1.9 nm. Line B exhibits a center wavelength of 0 nm and a linewidth of 0 nm put in correct numbers | |
| | (b) Spectrum of the same SiV center after pick-and-place, excited with the same laser as before. While Line A is almost gone, line B still exists and is the predominant line of the spectrum. Note: different longpass filters were used for the two measurements. Measurement (a) was performed with a 720 nm longpass filter, measurement (b) with a 710 nm longpass filter. | 18 |
| 2.9 | (a) Scan of the laser light stemming from the VCSEL Bm4 and the fluorescence light from the SiV center in the filter window 730 nm to 750 nm. (b) Scan of the laser light stemming from the VCSEL Bm2 without coupled SiV center. The outcome of the two scans is almost identical. | 19 |
| 2.10 | (a) Recorded Spectrum of the SiV center in the transferred nanodiamond on VCSEL Bm4 during VCSEL operation. No distinct SiV center lines are visible. (b) Recorded spectrum of VCSEL Bm2 (without SiV center) | 19 |
| 2.11 | Reflectivity of the Distributed Bragg reflector (DBR) of the VCSEL, and spectrum of the SiV center measured during VCSEL excitation. The reflectivity of the DBR and the VCSEL emission spectra are depicted with different scales. The shape of the measurement of the SiV center during VCSEL operation coincides with the shape of the DBR reflectivity. The spectrum of the SiV center is not visible. As the emission from the SiV center is small compared to the intensity of the laser sideband in the same wavelength regime, the SiV centers emission is not detectable warum schaut das spectrum anders aus als das, was einzeln geplottet ist? | |
| 2.12 | Picture recorded with a commercial high resolution laser scanning microscope. The area shaded in blue represents the photoluminescence scan in image (b). (b) Photoluminescence scan of a 8 $\mu\text{m} \times 13 \mu\text{m}$ | 20 |
| 2.13 | <caption> | 21 |
| 2.14 | Image of the sample surface of 100 nm wet-milled nanodiamonds spin-coated on an iridium substrate illuminated with diffuse white light. The white bars are the horizontal bars of the cross markers which serve as a coarse orientation on the sample surface, the white dots are nanodiamonds, the big black spot is an artifact. | 22 |
| 2.15 | | 23 |
| 2.16 | <caption> | 25 |
| 2.17 | | 25 |
| 2.18 | <caption> | 26 |
| 2.19 | <caption> | 27 |

| | | |
|----------------|-------|----|
| 2.20 <caption> | | 27 |
| 2.21 <caption> | | 27 |
| 2.22 <caption> | | 28 |
| 2.23 <caption> | | 28 |
| 2.24 <caption> | | 28 |

List of Tables

| | |
|--|---|
| 1.1 Classification of diamond synthesized by chemical vapor deposition | 4 |
|--|---|

Chapter 1

Silicon Vacancy Centers in Diamond

In the following we introduce color centers, i.e. optically active point-defects, present in a diamond lattice. We focus on color centers combining silicon impurities and lattice vacancies (SiV) in particular since their experimental study is at the focus of this thesis. We start by presenting the most important properties of diamond and emphasize its suitability as a host for optical applications with color centers. A classification of diamond with respects to defects and impurities as well as crystallinities serves as a preparation for the introduction of methods to synthesize diamonds containing SiV centers presented in ???. Finally, we discuss SiV centers in detail and focus on their most important optical properties as reliable single-photon sources at room temperature. In particular, we zoom in on the key features of its luminescence spectrum, the zero-phonon-line and the phonon side band. Our discussion partially follows the presentation in [1, 2, ?, 3].

1.1 Diamond as a host lattice

Diamond is a metastable modification of carbon which is, in fact, stable under normal pressure and at room temperature [4]. Carbon atoms form strong sp^3 -bonds with each other in a tetrahedral arrangement of neighboring atoms. The resulting sp^3 -hybridized lattice is of exceptional mechanical stability, making diamond the hardest known material [?]. The crystal structure can also be interpreted as a face-centered cubic (fcc) lattice with two carbon atoms in the primitive Bravais cell, situated at $(0, 0, 0)$ a and $(\frac{1}{4}, \frac{1}{4}, \frac{1}{4})$ a with $a = 3.567 \text{ \AA}$ denoting the lattice constant [5]. Figure 1.1 illustrates the structure.

The valence and conduction bands of diamond are separated energetically by a large direct band gap of 7.3 eV while its indirect band gap amounts to 5.5 eV [6, 7]. As a result diamonds are transparent for light of all wavelengths larger than 230 nm [8]. This transparent quality makes diamond an ideal host material for various optically active lattice defects or impurities. These induce a wide range of discrete energy levels accommodated by the sizable band gap. The absorption of optically active impurities or impurity complexes gives rise to the color of diamonds, thus these impurities are commonly termed color centers [2]. Due to the exceptional mechanical stability of diamond color centers too are very stable, another important property enabling optical applications.

A property of diamond, detrimental to some optical applications, is its large refractive index

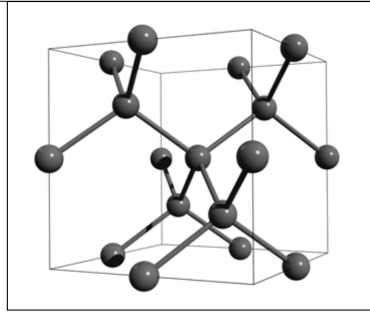


Figure 1.1: Face-centered cubic diamond lattice. Note the tetraedal arrangements of carbon atoms. Figure reproduced with permission from [1].

with values of 2.49 at 360 nm and 2.4 at 800 nm respectively [9]. Thus, a portion of the fluorescent light escaping from the diamond is reflected back into it, effectively reducing the efficiency of light extraction. If nanodiamonds smaller than the wavelength of the light to be collected are used, internal reflection is suppressed and the extraction efficiency can be increased [10].

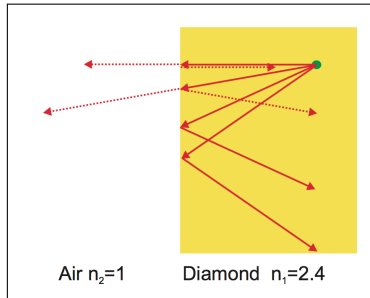


Figure 1.2: Light from a fluorescent emitter inside the diamond (green dot) undergoes reflection at the diamond-air interface. Figure reproduced with permission from [2].

1.2 Classification of diamond

Two major approaches for classifying diamond are commonly encountered. First, classification according to the presence or absence of certain impurities or impurity complexes. Second, classification based on different diamond crystallinities observed. In the following both classification systems are briefly introduced.

1.2.1 Classification by impurities

Impurities or complexes of impurities in the diamond lattice can be optically active and thus change the optical properties of diamond. Most strikingly perhaps is the appearance of color in otherwise colorless diamond due to a sufficient concentration of such defects. Using IR absorption spectroscopy the degree of nitrogen impurities can be determined. It is used to subdivide diamonds into distinct groups named Type I and Type II [11, 12]. The groups are further subdivided as follows:

- Type Ia: With a nitrogen concentration of up to 3000 ppm most natural occurring diamonds belong to this group [9]. Nitrogen appears arranged predominantly in aggregate clusters forming complexes of impurities. These complexes are optically active, absorbing light in the blue range of the visible spectrum. Consequently Type Ia diamonds often exhibit a yellow to brownish coloration.
- Type Ib: With concentrations of up to 500 ppm nitrogen atoms appear predominantly in isolation, replacing individual carbon atoms in the diamond lattice. In addition to absorbing visible blue light, green is being absorbed as well. Type Ib diamond thus exhibits intensified the yellow or brownish coloration. While only 0.1% of naturally occurring diamond fall into this class, almost all synthetic diamonds created using the high-pressure, high-temperature (HPHT) method are of Type Ib [9].

While Type I diamond exhibits an appreciable concentration of nitrogen, Type II diamonds lack nitrogen entirely. Type II diamond is divided into two subgroups according to the presence or absence of boron as follows:

- Type IIa: Can be considered pure as they lack boron impurities and other optically active defects [13]. They thus are colorless. Up to 2% of naturally occurring diamond and most diamonds synthetically created using the chemical vapor deposition (CVD) method are of Type IIa [9].
- Type IIb: Contains appreciable concentrations of boron atoms replacing individual carbon atoms in the diamond lattice. Boron defects are optically active absorbing visible light ranging from red to yellow. Depending on the Boron concentration blue to grey colorations are observed. Furthermore, diamond is turned from an insulator to a efficient p-type semiconductor in the presence of boron impurities [14].

We remark that for many modern applications of diamonds the presented "classic" categorisation of diamond is not enough. In these cases a precise quantification of the concentration and nature of various relevant impurities is called for [15, 16].

In this section we also briefly touched upon the CVD and HPHT methods, two approaches to synthetically produce diamonds. Both are relevant for this thesis and are explained in detail in ??.

1.2.2 Classification by crystallinity

Up until now, the discussion assumed that diamond forms a lattice consisting of one giant single crystal. However, other crystallinities are possible and can be used to classify diamond. They range from mono or single crystals to polycrystalline, nanocrystalline or even ultra-nanocrystalline diamond films [17]. This classification is particularly useful for synthesized diamond as will be discussed in ?. Table 1.1 summarizes the different sizes of diamonds or diamond films which can be achieved using variations of the CVD method.

Diamond films consist of isolated diamond grain of random orientation with sp² hybridized grain boundaries and graphit-like inclusions [1]. Carbon present in non-diamond phases, e.g. graphite or amorphous carbon gives rise to detrimental light absorption while crystal boundaries lead to increased scattering losses. As the size of diamond crystallites get smaller, the

ratio of non-diamond carbon to diamond carbon increases. Thus losses are most pronounced for the smallest grain diamond films.

Table 1.1: Classification of diamonds synthesized using CVD [3].

| Crystallinity | Grain size |
|-----------------------|---------------------------|
| monocrystalline | arbitrary |
| polycrystalline | 50 nm to 10 μm |
| nanocrystalline | 10 nm to 50 nm |
| ultra-nanocrystalline | < 10 nm |

1.3 Silicon-vacancy center

A color center is an optically active point-defect in a crystal lattice, capable of absorbing and emitting light. Defects can consist of one or several vacant lattice sites, foreign atoms replacing lattice atoms or a combination thereof. If the presence of a defect induces discrete energy levels located in the band gap of the host material, the color center can be interpreted as its own quantum system. In other words, the color center can be viewed as a single isolated and localized artificial atom embedded in a host matrix. As such it is able to absorb light and emit single photons by means of fluorescence.

Compared to alternative single photon sources like single atoms [18], Ions [19] or individual quantum dots [20, 21], color centers offer a couple of advantages due to their solid state environment. As a result of the high mechanical stability of the host lattice color centers exhibit increased photo-stability, in particular compared to organic molecules as light sources. Furthermore the host lattices offers protection for color centers from detrimental interactions with aggressive free molecules [22]. Lastly, color centers can be handled and investigated at room temperature, thus significantly reducing the experimental efforts necessary to study them.

Of particular interest are color centers as single photon sources when hosted in diamond. With its transparency, exceptional stability and minimal phononic interactions at room temperature the diamond lattice is an ideal host matrix for color centers [23, 24]. While more than 500 different color centers in diamond are documented, only a small fraction has been investigated with respect to their properties as single photon sources [9]. For an in-depth review of color centers and their versatile applications see [25, 26]. The two arguably most prominent examples of well-studied color centers are vacancy centers featuring nitrogen and silicon [27, 28, 29].

The silicon-vacancy (SiV) center in diamond and its properties is at the center of this thesis. The SiV center has been established as an efficient single photon source at room temperature. It shows very narrow emission lines with record count rates up to 6.2×10^6 cps (counts-per-second) [30]. The emission of indistinguishable photons and the optical access of electronic spin states have been demonstrated [31, 32, 33, 34], hinting at the possibility of deploying SiV centers as spin-qubits.

A silicon-vacancy center is formed in a diamond lattice by substituting two carbon atoms by a silicon atom and a nearby empty lattice site respectively. The silicon atom occupies its

energetically optimal position by sitting in-between two lattice sites. This is called “split-vacancy” configuration and induces a D_{3d} symmetry with the two vacancies and the impurity alligned along the $\langle 111 \rangle$ diamond axis [?], see Figure 1.3.

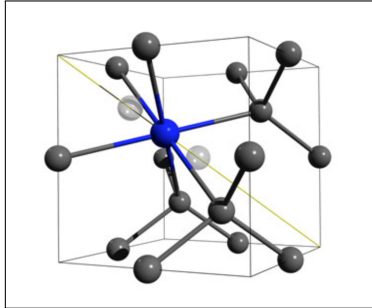


Figure 1.3: Crystal structure of the SiV center embedded into the diamond lattice: The silicon atom (blue sphere) sits in between two vacant lattice sites (white spheres) forming a “split-vacancy” configuration aligned along the $\langle 111 \rangle$ crystallographic axis (yellow line). Figure reproduced with permission from [1].

The SiV center is known to occur in two different charge states. The first is the neutral state or SiV^0 with a zero-phonon transition at 1.31 eV (946 nm). It is associated with a $S = 1$ ground state [35]. The second state is the negatively charged state SiV^- where the silicon-vacancy center recruited an additional free electron. It exhibits a zero-phonon transition at 1.68 eV (738 nm). Its ground state has been determined as a $S = \frac{1}{2}$ state [36, 37]. Due to its outstanding brightness and the location of the zero-phonon-line in the visible range of the spectrum, this thesis focuses on the negatively charged SiV center. For convenience we drop the charge distinction from now on and refer to SiV^- centers simply as SiV centers.

SiV centers have been created using CVD in nanodiamonds and single-crystal diamond films [38], see ?? for details. It is also possible to directly implant silicon atoms into pure diamond. High temperature annealing must then be used to animate present lattice vacancies to recombine with silicon impurities in order to form split-vacancy SiV centers [39, 37].

In the following sections we detail the most important luminescence properties of SiV centers in diamond. For a comprehensive review we refer to [1, 2] and references therein.

1.3.1 Luminescence properties

The silicon-vacancy center as a quasi-atomic system is capable of absorbing and emitting light. When a ground state electron absorbs a photon of appropriate energy, it is promoted to a discrete higher-energy excited state located within the band gap of the diamond host matrix. Reversing this excitation relaxes the electron back down to the ground state while emitting a so-called fluorescent photon, accounting for the energy difference between excited and ground state. This transition is “spin-allowed”, limiting the life-times of excited states to nano-seconds and thus promoting rapid relaxation and associated fluorescence [40].

Since fluorescence is directly linked to the electronic structure of the SiV center, see Figure 1.4. It follows that photoluminescence spectroscopy can be used to study it using a laser to optically excite the SiV center. In the context of this thesis, optical above-resonant excitation is the method of choice, in particular, when used in conjunction with a confocal photoluminescence

setup which will be discussed in ???. If the excitation energy exceeds the energy of the lowest excited state, electrons are promoted to higher electronic and vibrational states. Conveniently, these states relax rapidly towards the lowest excited state in non-radiative processes [40]. Once the lowest excited state is reached, a fluorescent transition can follow. It has been shown that above-resonant excitation is feasible for excitation energies ranging from 1.75 eV to 2.55 eV [?, 41, 42]. If the excitation energy is chosen too high, however, the SiV center is ionized. Electrons donated to the diamond conduction band do not participate in fluorescence. Ionization may be reversed if a positively charged SiV center manages to capture a free electron from the conduction band. This charge state conversion is believed to be linked to fluorescence intermittence, more intuitively named as blinking SiV centers [43, 44].

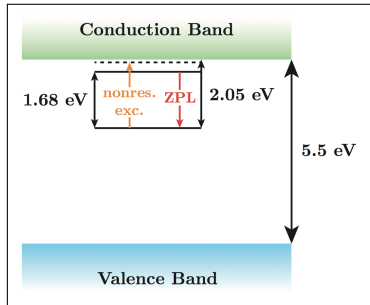


Figure 1.4: Simplified picture of the generous 5.5 eV band gap of diamond with discrete states induced by the presence of SiV centers. The SiV center ground state is situated 2.05 eV below the diamond conduction band. The lowest excited state sits 1.68 eV above the ground state with the zero-phonon-line transition in red connecting the two. Above-resonant optical excitation is indicated in orange. Figure courtesy of [?].

The fluorescence spectrum of SiV centers have two prominent features: A narrow zero-phonon-line and a broad phonon side band. The former is connected to fluorescent photons associated with a purely electronic transition while the latter involves vibrational transitions involving electron-phonon interactions. The phonon side band is typically shifted to higher wavelengths with respect to the zero-phonon-line. The resulting energy deficit can be explained by phonons being created during the relaxation of higher vibrational states. A shift in the opposite direction can also be observed in rare cases if phonons are absorbed during the relaxation process [?].

The relative strength of the zero-phonon-line and the phonon side band is connected to the electron-phonon coupling of the excited color center and thus to lattice vibrations. When a color center is excited, its charge distribution changes. As a result, the equilibrium positions of all particles involved in the color center shift leading to changes in color center geometry. Naturally, the combined changes of charge distribution and geometry of the color center affect the surrounding atoms of the host lattice. Similarly, if the excited state relaxes back to the ground state, the process occurs in reverse. Thus, due to differing atomic arrangements for ground and excited states, the emission and absorption of photons is accompanied by lattice vibrations, i.e. phonons. In other words, the electron-phonon interaction couples the motion of the lattice and electronic transitions of a color center [45, 46].

The Huang-Rhys model allows us to discuss the electron-phonon interaction in SiV centers in more detail. Our discussion follows the presentation in [47]. The model assumes in its simplest form that vibrational modes can be modelled as oscillations of nuclei between their

euilibrium coordinates q associated with the electronic states [1]. Let $\mathcal{K}_{^3A_2}(q)$ and $\mathcal{K}_{^3E}(q)$ denote the harmonic potentials of the ground and excited states respectively:

$$\mathcal{K}_{^3A_2}(q) = \frac{1}{2}\Omega^2 q^2 \quad (1.1)$$

$$\mathcal{K}_{^3E}(q) = C_{^3E} + aq + \frac{1}{2}(\Omega^2 + b)q^2 \quad (1.2)$$

$$= C_{^3E} - C_R + \frac{1}{2}(\Omega^2 + b)(q - \delta q)^2. \quad (1.3)$$

It follows that the vibrational modes of ground and exited states are given as harmonic states with discrete energies $\hbar\Omega(\nu + 2)$ as well as $\hbar\sqrt{\Omega + b}(\nu + 2)$ respectively, where ν denotes the occupation number and Ω the frequency. Further, let aq denote the linear nuclear displacement of the excited state configuration with respect to the ground state equilibrium where $q = 0$ holds. The quadratic term bq^2 refers to the vibrational frequency shift due to a redistribution of charge between the electronic states. Given the linear and quadratic electron-phonon coupling strengths a and b , the equilibrium displacement of the 3E state can be obtained as:

$$\delta q = \frac{-a}{\Omega^2 + b}, \quad (1.4)$$

while the relaxation energy reads [47]:

$$C_R = \frac{a^2}{2(\Omega^2 + b)} = \hbar S \sqrt{\Omega + b}, \quad (1.5)$$

where S is referred to as Huang-Rhys factor.

To reason about the probabilities of various transitions between different vibrational levels associated with ground and excited states, the Franck-Condon principle can be applied [?, ?]. It states that transitions between electronic states become more probable if origin and destination states have vibrational levels with similar energy. This implies that the most probable transitiobs occur between states requiring no change of nuclei positions. Figure 1.5 illustrates the application of the principle for the Huang-Rhys model.

We find that the most probable optical relaxation from an 3E excited state back to an 3A_2 ground state originates from the fundamental vibrational 3E state, i.e. the lowest-energy excited state. This state is shifted by δq with respect to the ground state, indicating that the energetically optimal nuclei positions differ from their ground state equilibrium positions. The most probable destination of the relaxation is a higher vibrational level of the 3A_2 ground state with similar nuclei positions. From there, electron-phonon interactions continue the relaxation process down to the fundamental vibrational level of the ground state. This non-radiative process allows nuclei to return to their original ground staet equilibrium positions. The process of exciting the system from the ground state, proceeds in reverse. The most probable optical excitation promotes an electron from the fundamental 3A_2 ground state to a higher vibrational level of the 3E excited state. The optical transition is such that nuclei positions do not change. Note that optical transitions are faster than vibrational transitions since they do not require a change in nuclei positions. Once in the higher vibrational excited

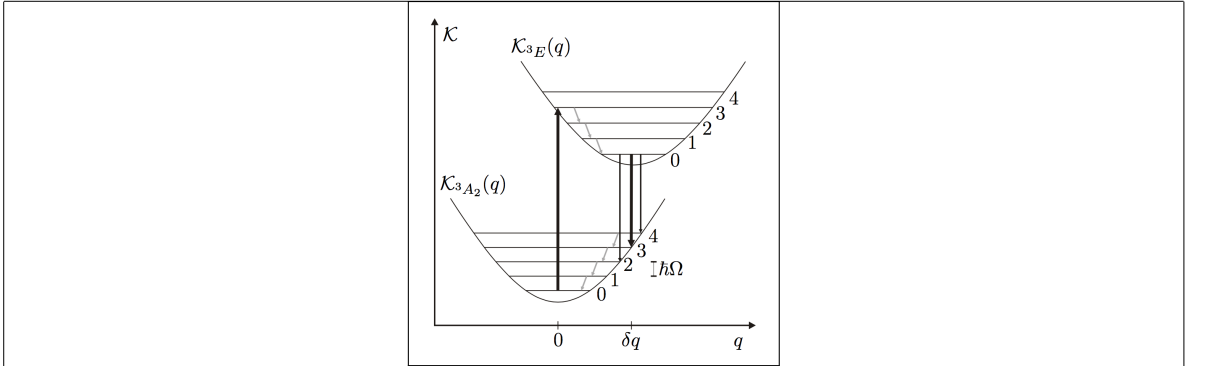


Figure 1.5: Huang-Rhys model of the vibrational transitions in the Frank-Condon picture: The excited state $\mathcal{K}_{3E}(q)$ is shifted by δq with respect to the ground state potential $\mathcal{K}_{3A_2}(q)$. The recombination originating at δq marks the most probable transition (thick black arrow) from the fundamental 3E vibrational level to one of the vibrational levels of the 3A_2 ground state followed by non-radiative transitions to the equilibrium position $q = 0$. The number of vibrational quanta involved in an optical transition are determined by the Huang-Rhys factor S . The excitation reverses the process. Optical transitions occur between states with identical values of q and are shown as vertical black arrows. Non-radiative transitions change the value of q and are shown as angled gray arrows. Figure and caption reproduced with permission [1].

state, electron-phonon interactions mediate a transition down to the fundamental 3E excited state with an associated change in nuclei positions. From there the relaxation-excitation cycle and its induced periodic changes in nuclei positions repeats.

As discussed, transitions involving phonons mostly originate from the fundamental vibrational level of excited electronic states and end in higher vibrational states of the electronic ground state. Photons emitted during the relaxation process are associated with the phonon side band of the SiV center. The observed red-shift of the phonon side band is directly tied to the phonon energy with higher order sidebands showing multiples of this energy. Note that the The Huang-Rhys factor S can be interpreted as an indicator of the most probable optical transition involving photons. Thus, it can be used to quantify the strength of the electron-phonon interactions in SiV centers. A small value of S indicates a weak electron-phonon coupling resulting in negligible phonon side band emmisions. If no phonons are involved, the entire emission is concentrated in the zero-phonon-line. Conversely, a large value of S indicates extensive electron-phonon interactions, leading to a pronounced phonon side band and a weaker zero-phonon-line. This dependence is naturally described by

$$\frac{I_{ZPL}}{I_{ZPL} + I_{PSB}} \quad (1.6)$$

For SiV centers hosted in polycrystalline diamonds the Huang-Rhys factors have been determined to be very small ranging from 0.08 to 0.24 [48, 21, 49]. As a result the zero-phonon-line as the most probable transition dominates the luminescence spectrum making SiV centers excellent narrow-band emitters. Figure 1.6 illustrates the stark difference between the zero-phonon-line and the phonon side band. In contrast, $S = 3.74$ has been established for nitrogen vacancy centers [45]. A electron-phonon coupling of this magnitude concentrates almost all

emission into the phonon side band and leaves the zero-phonon-line almost indetectable.

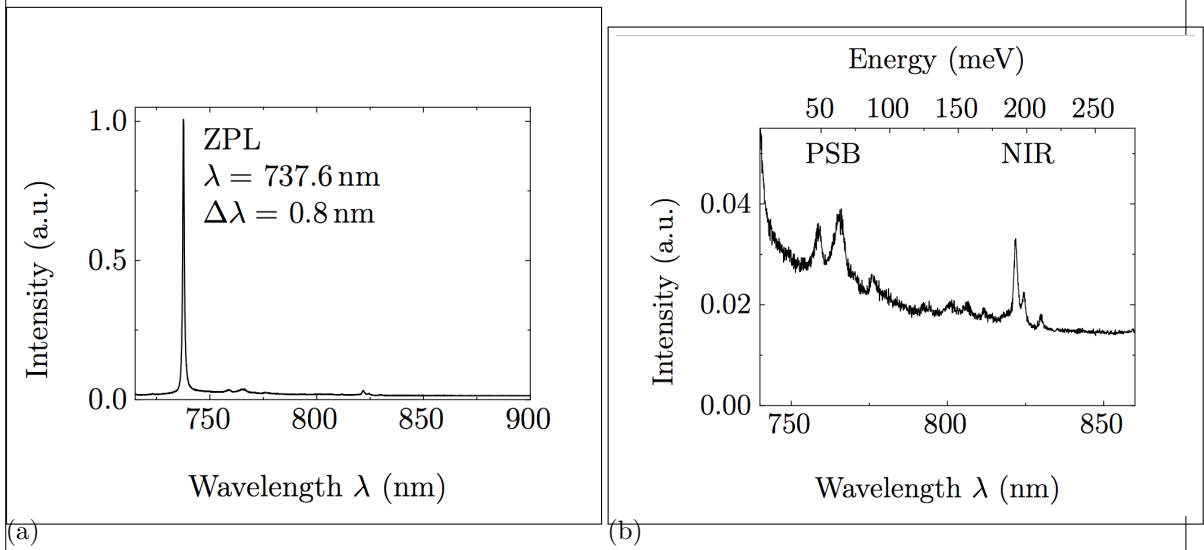


Figure 1.6: (a) The narrow zero-phonon-line dominates the luminescence spectrum. (b) Low intensity phonon side band shows distinct vibrational transitions. Figure reproduced with permission [1].

As an alternative measure for the electron-phonon coupling the Debeye-Waller factor can be used. It is closely related to the Huang-Rhys factor and defined as

$$D_w = e^{-S}, \quad (1.7)$$

which can be interpreted as the fraction of total photons that are emitted into the zero-phonon-line.

We remark at this point, that our discussion based on the Huang-Rhys model is assumed that only one vibrational mode couples to the color center which is a strong assumption. In general it is believed that in a solid state host matrix a discrimination between the modes of the undisturbed lattice and quasi-local impurity-induced modes is appropriate [46, 50, 51]. Furthermore, various mechanical properties such as stress in the lattice are reported to affect phonon energies [52]. In addition electron-phonon interactions and thus phonon side band features are believed to depend strongly on various local properties of color centers [53, 54]. Thus it is possible to encounter varying phonon side band features from one SiV center to the next. For a more detailed discussion of these effects we refer the reader to [2, 1] and references therein.

We close this chapter with a short discussion of the luminescence spectra of SiV centers at cryogenic temperatures. Naturally as temperatures approach absolute-zero the phonon side band must disappear. If SiV centers are cooled below $\approx 110\text{ K}$ a fine structure is revealed [?]. It includes up to 12 different lines with intensities proportional to the natural abundance of the three stable isotopes of silicon ^{28}Si , ^{29}Si , ^{30}Si [55]. Each isotope is associated with 4 lines attributed to doublet levels of ground and excited states which are split by 0.2 meV and 1.07 meV respectively [56, 37, 55]. The splitting itself is believed to be a result of spin-orbit coupling with a weak contribution of the dynamic Jahn-Teller effect [37]. Initial results were

based on ensembles of SiV centers, however, recently the splitting was detected for isolated SiV centers as well [57]. Figure 1.7 shows exemplary spectra representative for ensembles and single SiV center at cryogenic temperatures.

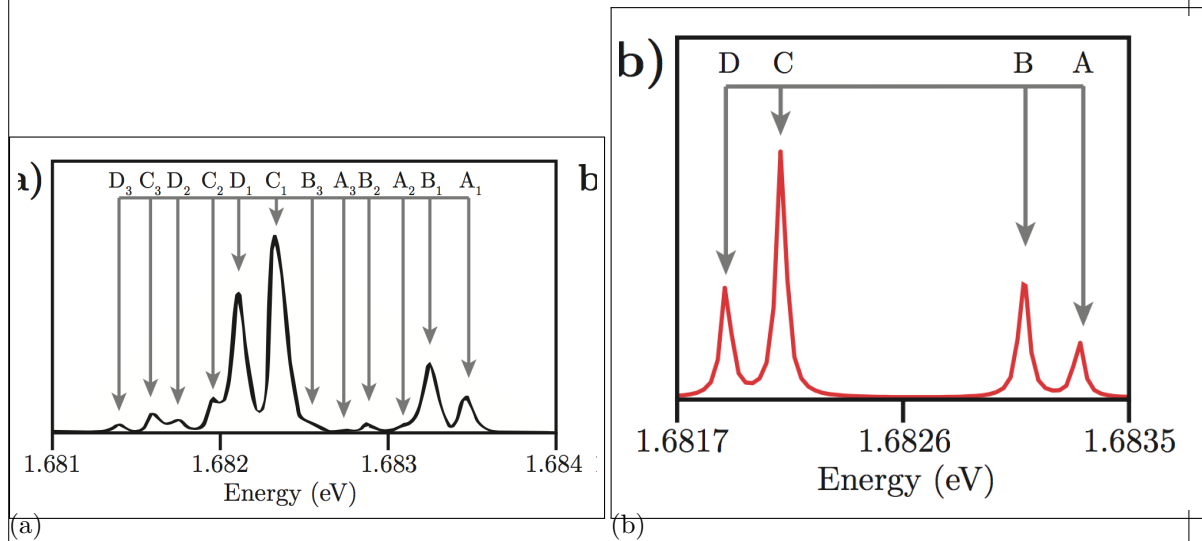


Figure 1.7: (a) Fluorescence spectrum of an ensemble of SiV centers at 10 K. 12 peaks can be seen, 4 for each stable isotope of silicon [?]. (b) Fluorescence spectrum of an isolated SiV center at 15 K. 4 peaks can be seen, 2 for the ground state and 2 for the excited state. Figure reproduced from [1].

Chapter 2

Coupling Nanodiamonds to Photonic Structures

In the last chapter, we saw that the spectroscopic properties of SiV centers vary strongly among individual nanodiamonds. Nanodiamonds are further implemented in photonic structures for the application in metrology as well as in quantum cryptography or quantum computing. Therefore, it is important to have a good knowledge of the spectroscopic properties of the individual SiV center. A preselection of nanodiamonds including an SiV center with optimal properties is performed. These properties contain both spectroscopic parameters as well as technical parameters for the pick-and-place process. Spectroscopic parameters contain narrow linewidth, high countrates and single photon emission, the technical parameters include a size of the nanodiamonds hosting the SiV center bigger than 70 nm and how isolated they lie on the substrate surface. The selected nanodiamond is then transferred to a target structure. In the scope of this thesis, nanodiamonds including SiV centers were coupled to two different kinds of structures:

- Vertical-Cavity Surface Emitting Lasers: The aim is to create a hybrid-integrated single photon source, where an electric current is employed to create single photons. The diamond containing an SiV center is placed directly on the beam output. Hence the SiV center is directly pumped by the laser beam. As the SiV center emits in another wavelength regime than the pump laser, the single photons are accessible after filtering the VCSEL laser light. This single photon source is interesting for metrological applications, as it is the major building block for a portable device ready to calibrate single photon detectors.
- Plasmonic Nanoantennas: The aim is to enhance photoluminescence intensity. As described in previous chapters, not only ZPL position and linewidth, but also the photoluminescence intensity varies strongly among individual SiV centers. However, in metrology a photon flux rate high enough to be measured by a low optical flux detector is needed [58]. This increase in intensity is achieved by coupling the SiV centers in nanodiamonds to plasmonic antennas. Furthermore, plasmonic antennas can be used to tune the emitters' photoluminescence spectrum.

think
of other
word

2.1 Additional Experimental Methods

To couple nanodiamonds to photonic structures, we pursued several different methods:

1. Directly spin-coat the structures with a nanodiamond solution and consecutively look for a structure containing a nanodiamond with an SiV center exhibiting the desired spectroscopic properties. This method was tried with the antenna structures, as there are many antenna structures on one substrate (see Figure 2.13a), therefore there is a chance that a suited nanodiamond is incidentally ends up at the right spot. However, it is not suitable for the VCSELs, first because of the morphology of the VCSELs and secondly, because there is a very limited number of VCSELs on one substrate.
2. Use an iridium substrate covered with nanodiamonds containing SiV centers, look for a suited nanodiamond and transfer it with a pick-and-place technique using a nanomanipulator. The nanomanipulator is essentially a thin tip in a scanning electron microscopy. The iridium substrate is preprocessed with markers, to record the position of the preselected nanodiamond. The huge advantage is that the very best suited nanodiamond can be preselected. However, disadvantages of this process include the electron radiation during the pick-and-place process, which might affect SiV center fluorescence light and the further restriction that the nanodiamonds must be big enough to be picked up with the nanomanipulator.
3. Similar to method 2, however the transfer is performed with an atomic force microscope. While this method has the advantage that the nanodiamonds are not irradiated with electrons, the disadvantage is that it is not possible to observe the picking process in real time. The area of the preselected nanodiamond has to be scanned after every pick-up try, which is very time consuming and therefore was not further pursued after some trials.

In the following paragraphs, the pick-and-place technique of method 2 is described in more detail. It is the coupling method most extensively deployed in the scope of this thesis and requires a range of experimental setups. The pick-and-place process was carried out with major help from C. Pauly, group of xxx Mücklich, Saarland University. The nanomanipulator setup was provided by the same group.

2.1.1 Nanomanipulator

In general, nanomanipulator is a tip mounted inside an SEM, allowing manipulation and visualization of the manipulation process at the same time. The one used for our experiments was built by the company Kleindiek (model MM3A-EM) and has a changeable tungsten tip (see Figure 2.1b). It is mounted inside a Thermo Scientific™ Helios NanoLab™ DualBeam™ microscope, which combines a focussed ion beam and an electron microscope. The bent nanomanipulator tip has 3 degrees of freedom: up/down and left/right both in an arc up to 240° and 12 mm in/out (see arrows in Figure 2.1b). Before nanomanipulation the tip was "sharpened" with the focussed ion beam by etching away tungsten with gallium ions. This sharpening was performed to meet the size criteria necessary to pick up the nanodiamonds. In Figure 2.3a the sharpened tip is shown (the radius of curvature amounts to 100 nm). The small tip sticking out of the bigger cone is the sharp tip used for pick-and-place.

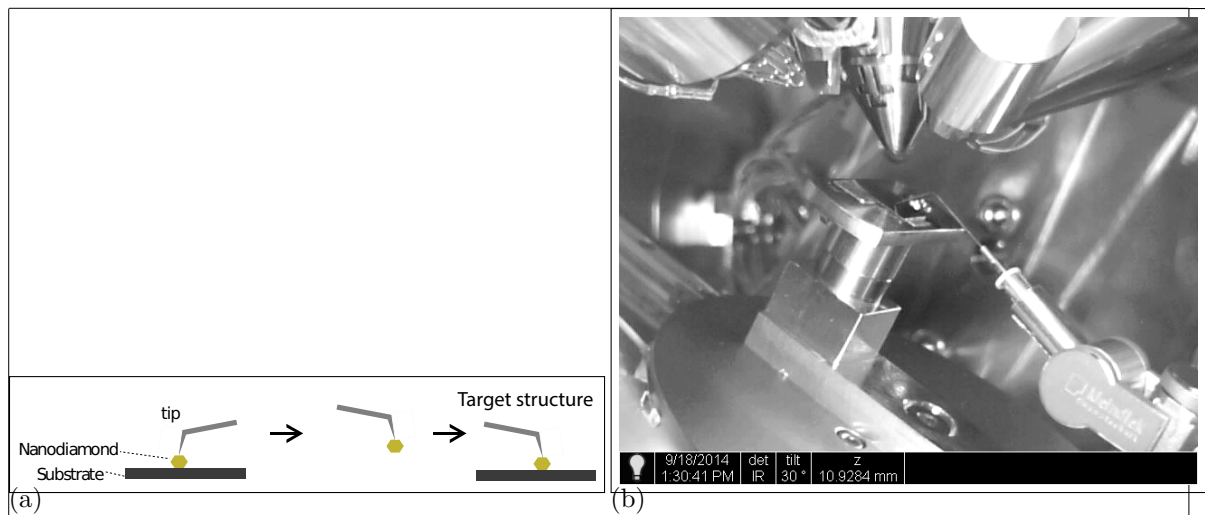


Figure 2.1: (a) Sketch of the pick-and-place process exploiting a nanomanipulator. (b) Image of the nanomanipulator mounted in the FIB. The arrows indicate the degrees of freedom of motion of the nanomanipulator. The custom made workbench is situated in the middle of the picture. On top of it, there is a 1cm^2 substrate with coated nanodiamonds, the nanomanipulator tip pointing to the middle of it. Behind it, there is the target vertical-cavity surface emitting laser. Perpendicular to the workbench, the objective of the electron microscope can be seen. The pointier cone perpendicular to the image top image edge is the objective of the focussed ion beam.

2.1.2 Determination of The Position of Nanodiamonds

An nanodiamond pre-characterized in the confocal setup exhibiting the preferred spectroscopic properties has to be found again in the SEM setup where the nanomanipulator is installed. Therefore, we milled cross markers into the iridium coating of the silicon substrate using the focussed ion beam prior to spin-coating the substrate with nanodiamond solution. The crosses' size is $10 \times 10 \mu\text{m}^2$ are exhibit a nominal depth of 40 nm. Four crosses are the cornerpoints of a $50 \times 50 \mu\text{m}^2$ square. The 10×10 crosses spaned one field of crosses; we usually put 3 fields of crosses on one substrate.

To record the position of a nanodiamond with respect to a cross marker, we used two different methods:

- Scanning the sample in the confocal setup while a white light source illuminates the sample from the side in an acute angle. The edges of the cross markers are visible in the fluorescence scan. After turning the white light lamp off, the same area is scanned once more to record the fluorescence from the SiV centers. An overlay of the two images identifies the position of fluorescent SiV centers with respect to the cross markers. The disadvantage of this method is, that it takes a lot of time, as every scan has to be performed twice. Also, as only fluorescence light scans are performed, no information of the nanodiamonds is accessible. Such information comprises of the size of the individual nanodiamonds and whether the nanodiamonds lie isolated on the substrate surface. These parameters are only available during the pick-and-place process in the SEM. An emitter with optimal optical properties can turn out not to be suited for pick-and-place just before the process itself, hence the time spent to optically characterize an emitter

fib pa-
rameter

put in
a pic of
white-
lightscan

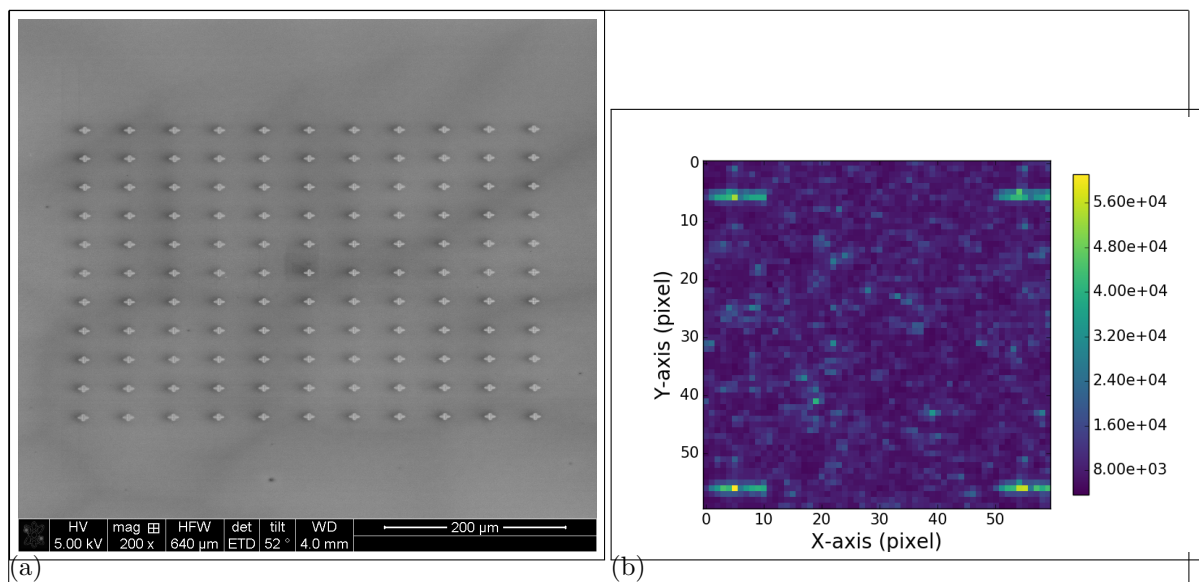


Figure 2.2: (a) Overview of a field of cross markers. The field spans 0.5×0.5 mm (b) White light scan of an area with a cross marker in all four corners.

was in vain.

- A more efficient method is scanning the substrate first in a commercial laser scanning microscope . The laser scanning microscope is a confocal microscope where the focus of a laser is used to obtain the height of a structure. It is possible to scan a whole field of cross markers in several minutes. The obtained image is a greyscale image, where the greyscale corresponds to the height deviation of a structure. Therefore, both the crosses and the nanodiamonds appear in darker shades of grey. So in contrast to the previous method, information on the size and isolation of the nanodiamonds is accessible. After scanning the substrate with the laser scanning microscope, it is put into the confocal setup. While observing the surface with the CCD camera (Figure 2.17), a specific cross marker is chosen as the starting point of a fluorescence light scan. Comparing the laser scanning microscope image and a fluorescence light scan, fluorescent dots of the fluorescence light scan are attributed to nanodiamonds in the laser scanning microscope scan (see Figures 2.12a and 2.12b).

specs
verify
info

2.1.3 The Pick-And-Place Process

After we identified nanodiamonds as well-suited for transfer to the target structure, both the substrate with the nanodiamonds and the target structure were mounted inside the SEM. The process was performed using a high resolution mode with a low acceleration voltage of the SEM of 1 keV and a current of 1.7 nA. The tip is approached to the pre-selected nanodiamond from above. As the SEM objective is mounted above the nanomanipulator, the proximity the nanomanipulator tip to the nanodiamond is not observable. The proximity is indirectly estimated by the shadow the tip casts onto the substrate and the focus. The first method is used for the coarse approachment of the tip to the nanodiamond: The closer the tip gets to the nanodiamond, the closer the shadow of the tip coincides with the nanodia-

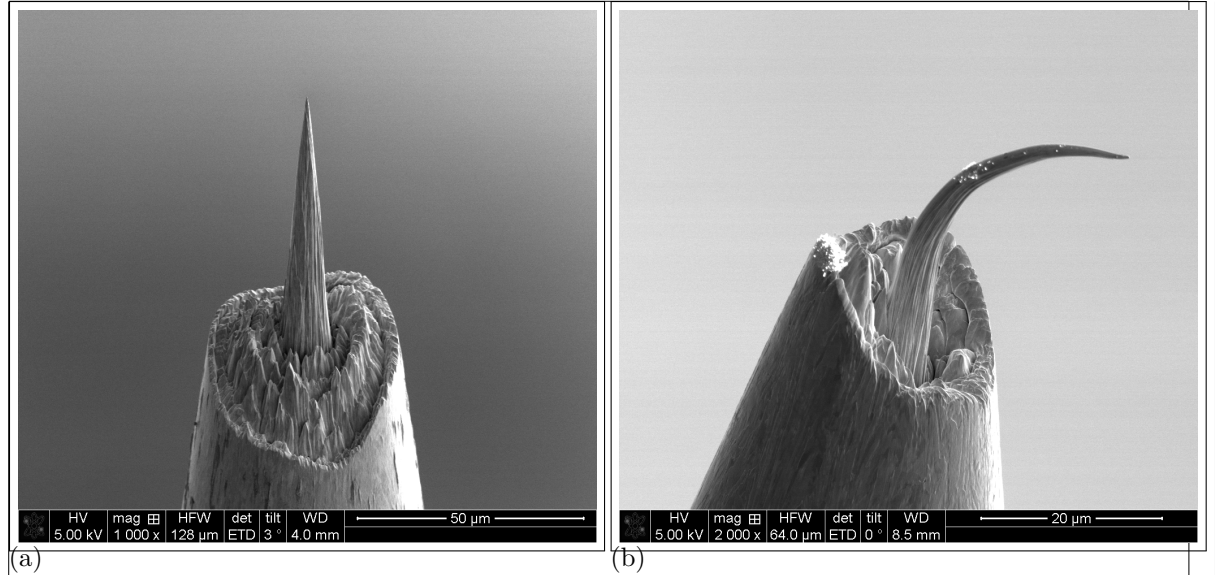


Figure 2.3

mond position. Exploiting the focus as an estimate for the proximity of the tip is used for fine adjustment during the last stage of the approachment. This is done as follows: At the end of the coarse movement, the tip of the nanomanipulator is still some distance above the nanodiamond. The SEM is focused on the nanodiamond, therefore the nanomanipulator tip is out of focus and appears blurry. As the tip is approached, it moves further and further into focus, its image becoming sharper, until the it touches the nanodiamond. As this is a tricky process, sometimes the tip was approached with too much force and was destroyed in the process (Figure 2.3b).

When performed correctly, due to adhesion, the nanodiamond sticks to the nanomanipulator tip when the both get in contact (Figure 2.15a). The nanomanipulator is then moved to the target structure and the same approachment procedure is applied. Dependent on the material of the target structure, the nanodiamond either sticks to the structure right away due to higher adhesion forces between the nanodiamond and the structure (as is the case for the golden plasmonic antennas). Or the nanodiamond has to be "wiped off" of the nanomanipulator tip in a sideways motion. In either way it is possible to place the nanodiamond within a precision of a few nanometers.

2.2 Coupling SiV centers to Vertical-Cavity Surface Emitting Lasers

For metrology, the photon flux rate has to be high enough to be measured by a low optical flux detector [58].

The red AlGaInP-based oxide-confined vertical-cavity surface emitting lasers (VCSEL) are compact and perfect candidates for excitation of SiV centers in a hybrid integrated single photon source: They exhibit wavelengths around 650 nm at continuous wave emission. SiV centers exhibit intensity maxima at an excitation at 670 nm and 690 nm [6]. In addition, VCSELs

diagram
einfuegen

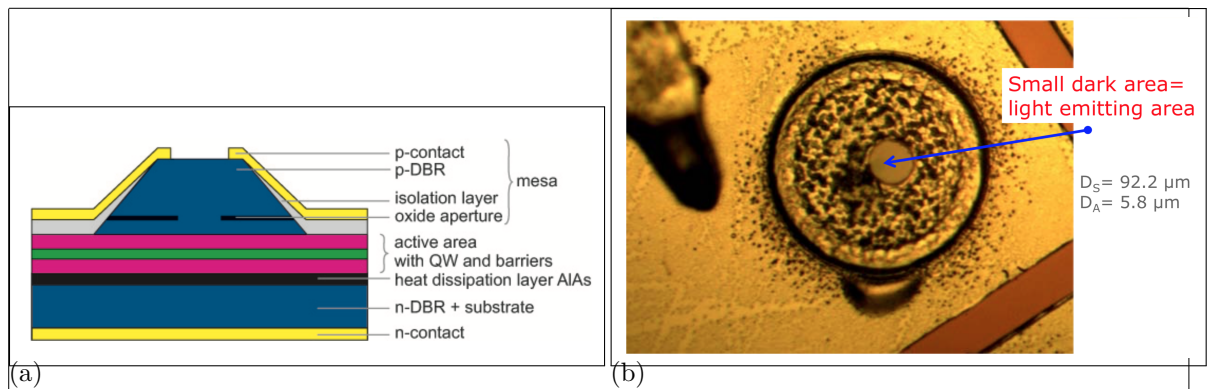


Figure 2.4: (a) Sketch of the VCSEL showing the different layers.

ask how to cite

(b) Image of the VCSEL. The circle with the black dots is the hole in the p-contact (diameter D_s , the smaller darker area in the middle is the laser output area (diameter D_A)

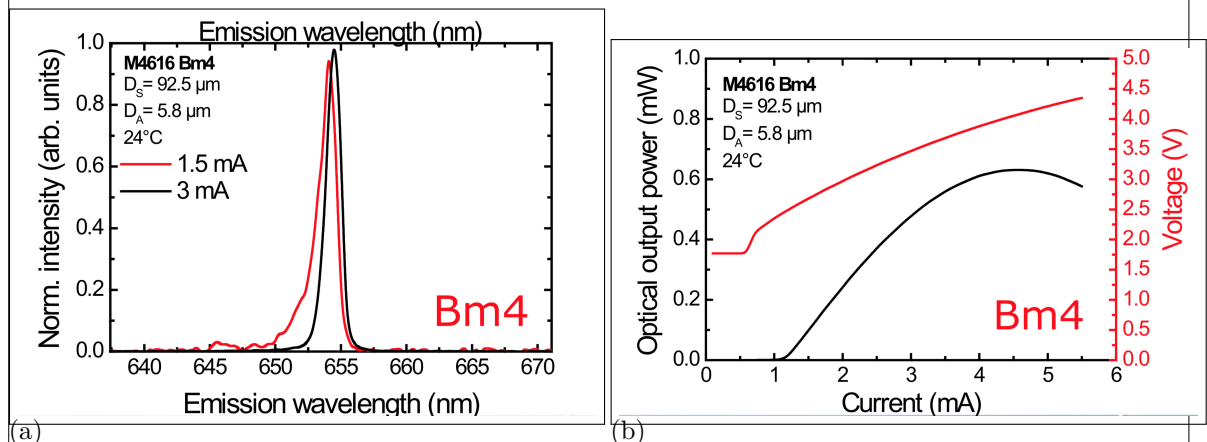


Figure 2.5: (a) Emission spectrum of the used VCSEL at two different currents. (b) Optical output power and voltage of the same VCSEL in dependence of input current. []

exhibit circular beam profile, have low divergence angle and emit linearly polarized light.

2.2.1 Vertical-Cavity Surface Emitting Laser Structure

The VCSEL structure (??) consists of an active region between two distributed Bragg reflectors (DBR). The bottom n-type DBR is made of 50 pairs of AlAs/Al_{0.5}Ga_{0.5}As, the p-type DBR consists of 36 Al_{0.95}Ga_{0.05}As/Al_{0.5}Ga_{0.5}As mirror pairs [59]. The active region consists of four GaInP quantum wells (QW). An oxide aperture in a field node of the standing wave serves as a spatial filter for maximum modal gain by confining the current and the optical mode. The active diameter which is defined by the oxide aperture amounts to 5.8 μm. As this region is the area where the laser emission exits the VCSEL, the nanodiamonds have to be put within this area. The used VCSEL exhibits an optical output power up to 1 mW with low threshold current of up to 3 mA at about 655 nm.

ist das
up to

nachdenken
wie for-
mulierung
richtig
ist

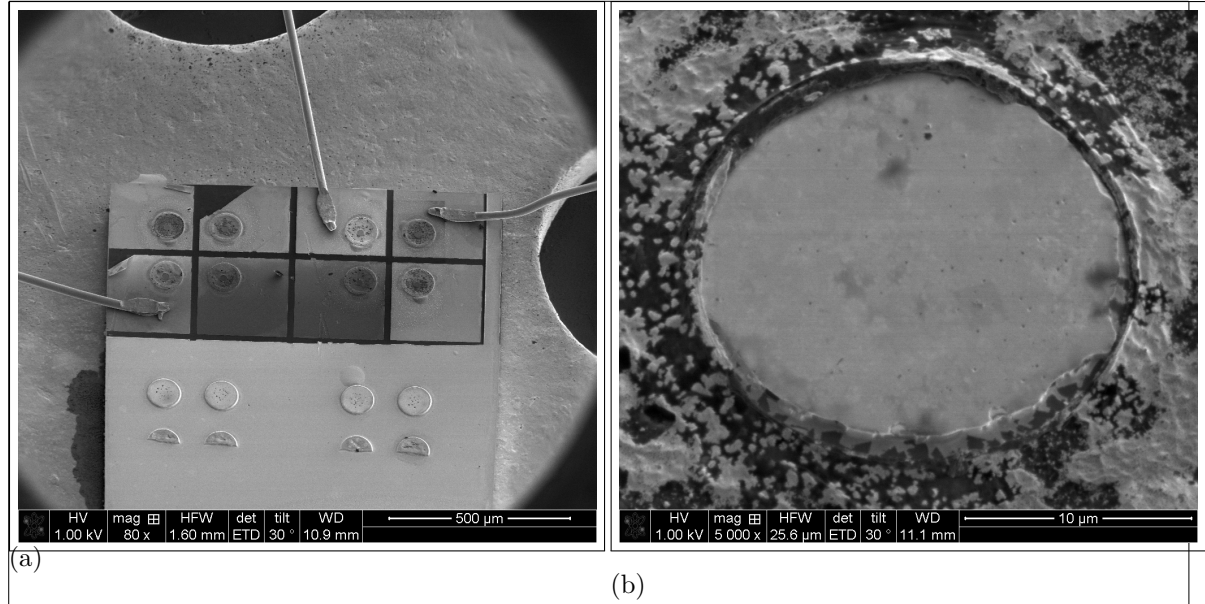


Figure 2.6: (a) SEM image of an array of VCSELs. The three wires are the anodes, which are connected to the top layer (p-contact) of the VCSEL. Therefore, three of the VCSEL structures can be operated. (b) Detail SEM image of the top of the exploited VCSEL Bm4. The circular middle part is the hole in the p-contact through which the top DBR is visible. The active diameter is smaller than that and not visible in the SEM.

2.2.2 SiV center in a Vertical-Cavity Surface Emitting Laser

As diamond material we used CVD grown nanodiamonds. They had been grown on an iridium coated silicon wafer (see ??). These nanodiamonds exhibit a nominal size of 200 nm. First, we selected a nanodiamond which exhibited one dominant line at 746.0 nm with a linewidth of 1.9 nm. Consecutively, its position on the substrate was determined using a white light laser scan as described in ?? . It was then transferred to the VCSEL Bm4 described in ?? . After a successful transfer of the pre-selected nanodiamond onto the active area of VCSEL Bm4, the VCSEL was put in the confocal setup. Using the laser from the confocal setup we checked if the pick-and-place process caused any modification of the spectroscopic properties of the SiV center such as a decrease of countrate or a modification of the fluorescence light spectrum. For this, the VCSEL itself was not operated itself. First, the VCSEL surface was scanned Figure 2.7a. A bright dot exhibiting a countrate of a few thousand counts per second is visible where the nanodiamond containing an SiV was put. A comparative scan of a VCSEL without nanodiamond only exhibits a background countrate, as expected (Figure 2.7b). The spectrum of the SiV center in the transferred nanodiamond was investigated before and after the pick-and-place process (Figure 2.8). The original spectrum before nanodiamond transfer exhibits a sharp line at 746.0 nm (denoted line A). After the pick-and-place process, this line is still there, albeit with a low intensity. Another line at 0 nm (denoted line B) which was a minor feature in the spectrum before pick-and-place, is the predominant line after the process. This modification of the spectrum is caused by a reduction of the intensity of line A and constant intensity of line B. The reduction of the intensity of line A may be caused by damage of the color center due to electron radiation. While the energy of the electrons is low compared to the ionization energy of the color center , we observed a reduction of fluorescence

was it
single?

check
number

numbers

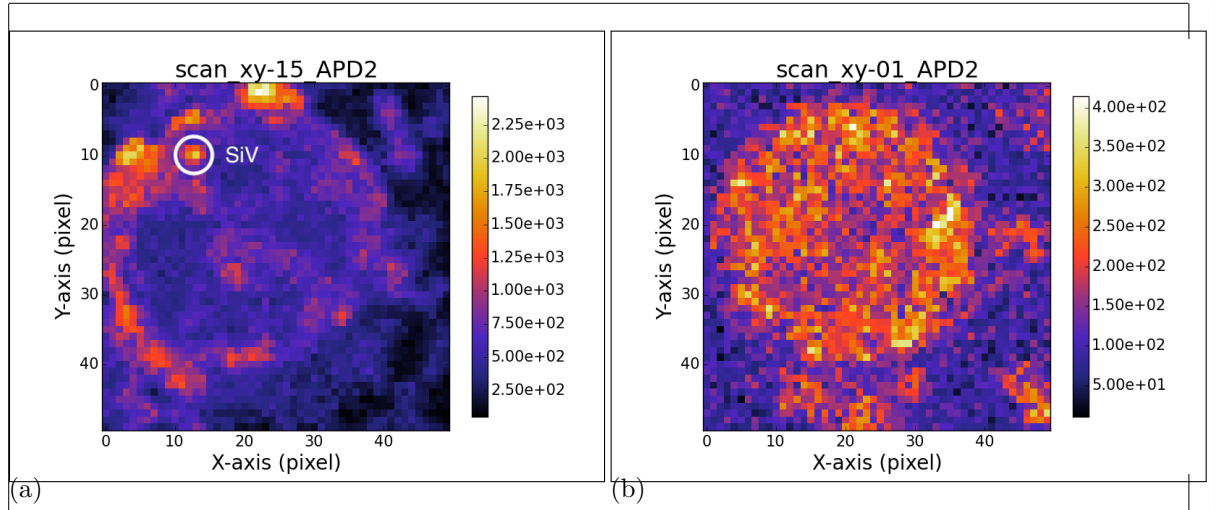


Figure 2.7: (a) Scan of the VCSEL Bm4 with coupled nanodiamond under excitation with the laser from the confocal setup. The big visible ring is the edge of the circular hole in the p-contact. The bright spot in the upper left corner corresponds to the transferred nanodiamond containing an SiV center. (b) Scan of the VCSEL Bm2 without nanodiamond under excitation with the laser from the confocal setup. The circular hole in the p-contact exhibits a constant countrate.

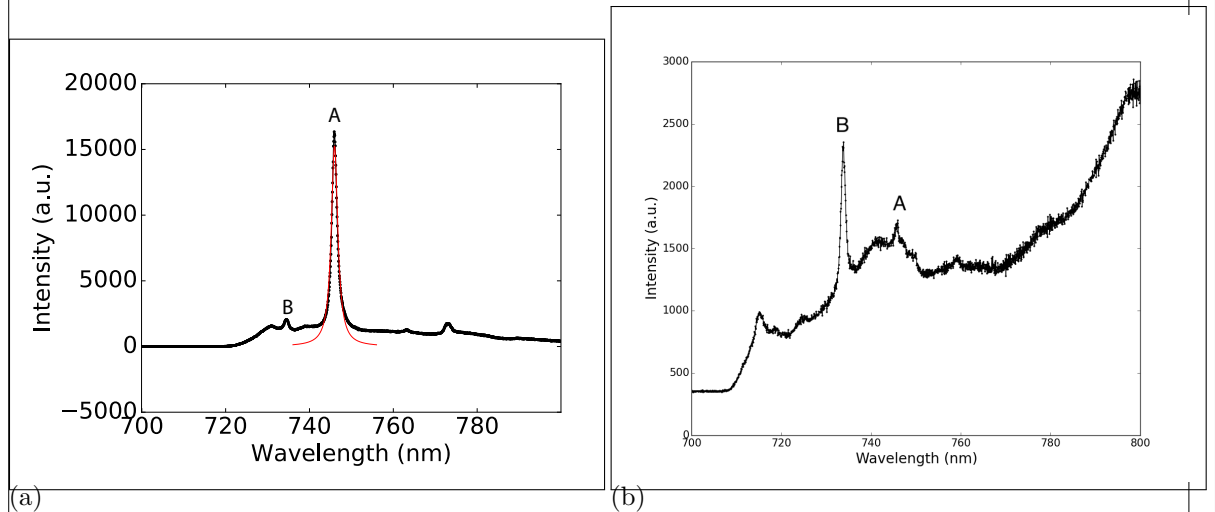


Figure 2.8: (a) Spectrum of the preselected diamond for transfer onto VCSEL Bm4 before pick-and-place. The strong line denoted A exhibits a center wavelength of 746.0 nm and a linewidth of 1.9 nm. Line B exhibits a center wavelength of 0 nm and a linewidth of 0 nm

put in correct numbers

(b) Spectrum of the same SiV center after pick-and-place, excited with the same laser as before. While Line A is almost gone, line B still exists and is the predominant line of the spectrum. Note: different longpass filters were used for the two measurements. Measurement (a) was performed with a 720 nm longpass filter, measurement (b) with a 710 nm longpass filter.

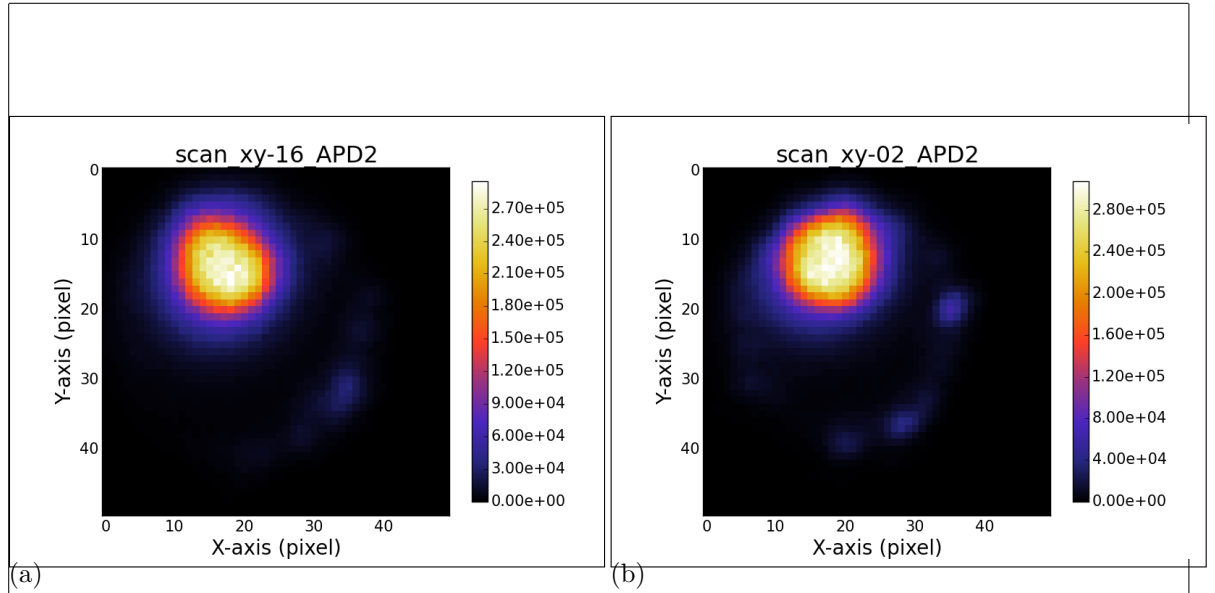


Figure 2.9: (a) Scan of the laser light stemming from the VCSEL Bm4 and the fluorescence light from the SiV center in the filter window 730 nm to 750 nm. (b) Scan of the laser light stemming from the VCSEL Bm2 without coupled SiV center. The outcome of the two scans is almost identical.

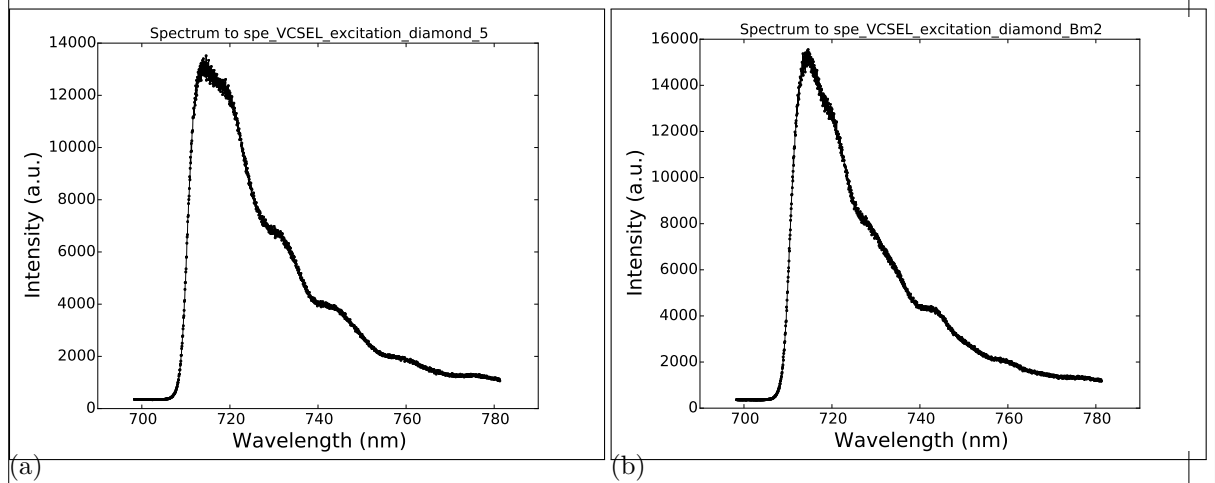


Figure 2.10: (a) Recorded Spectrum of the SiV center in the transferred nanodiamond on VCSEL Bm4 during VCSEL operation. No distinct SiV center lines are visible. (b) Recorded spectrum of VCSEL Bm2 (without SiV center)

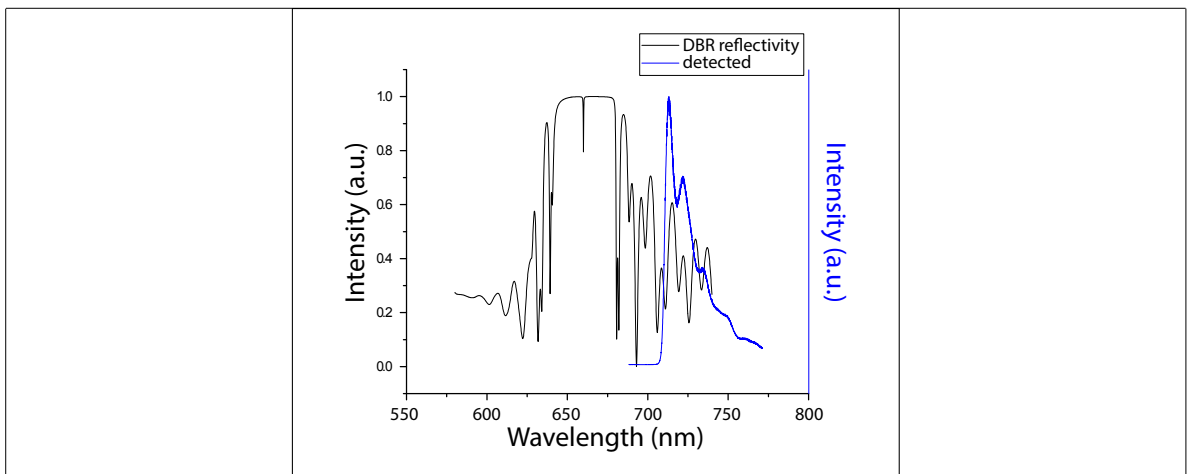


Figure 2.11: Reflectivity of the Distributed Bragg reflector (DBR) of the VCSEL, and spectrum of the SiV center measured during VCSEL excitation. The reflectivity of the DBR and the VCSEL emission spectra are depicted with different scales. The shape of the measurement of the SiV center during VCSEL operation coincides with the shape of the DBR reflectivity. The spectrum of the SiV center is not visible. As the emission from the SiV center is small compared to the intensity of the laser sideband in the same wavelength regime, the SiV centers emission is not detectable

warum schaut das spectrum anders aus als das, was einzeln geplottet ist?

light intensity after electron radiation (for a detailed description of this effect, refer to [?]). We then operated the VCSEL at 0.84 mA and 3.3 V and turned off the laser of the confocal setup. We scanned both the surface of VCSEL Bm4 (with nanodiamond) and of VCSEL Bm2 (without nanodiamond) with a 730 nm to 750 nm bandpass filter. This filter window suppresses the VCSEL laser line at 655 nm (2.5a) while leaving the SiV center emission nearly unchanged. The light areas in Figure 2.9 correspond to the laser output areas. We measured a spectrum at the same points as before VCSEL operation. In the case of VCSEL Bm4, this spot corresponds to the position of the SiV center. The following observations are made from the measurements:

- In both scans, the laser output area is visible as a big bright spot. There is no difference in intensity between VCSEL Bm4 and Bm2.
- The spectra of VCSEL Bm4 and Bm2 are almost identical.

The spectrum recorded in the confocal setup corresponds well with the DBR reflectivity (Figure 2.11). Hence, we conclude, that the detected emission is due to the VCSEL and does not stem from the SiV center. From these observations, we draw the conclusion that the fluorescence light emission from the SiV center is small compared to the sideband of the VCSEL emission in the wavelength regime where the SiV center emission is expected. Therefore, the SiV center emission is not detectable during VCSEL excitation.

Ongoing work is performed to reduce sideband emission of the VCSEL in the SiV center emission regime. A promising approach is to add a gold layer on top of the VCSEL which acts as a tunable mirror. While films of gold have a transmittance maximum at 500 nm, the

besser
begruen-
den, was
passiert

ev besser
begruen-
den

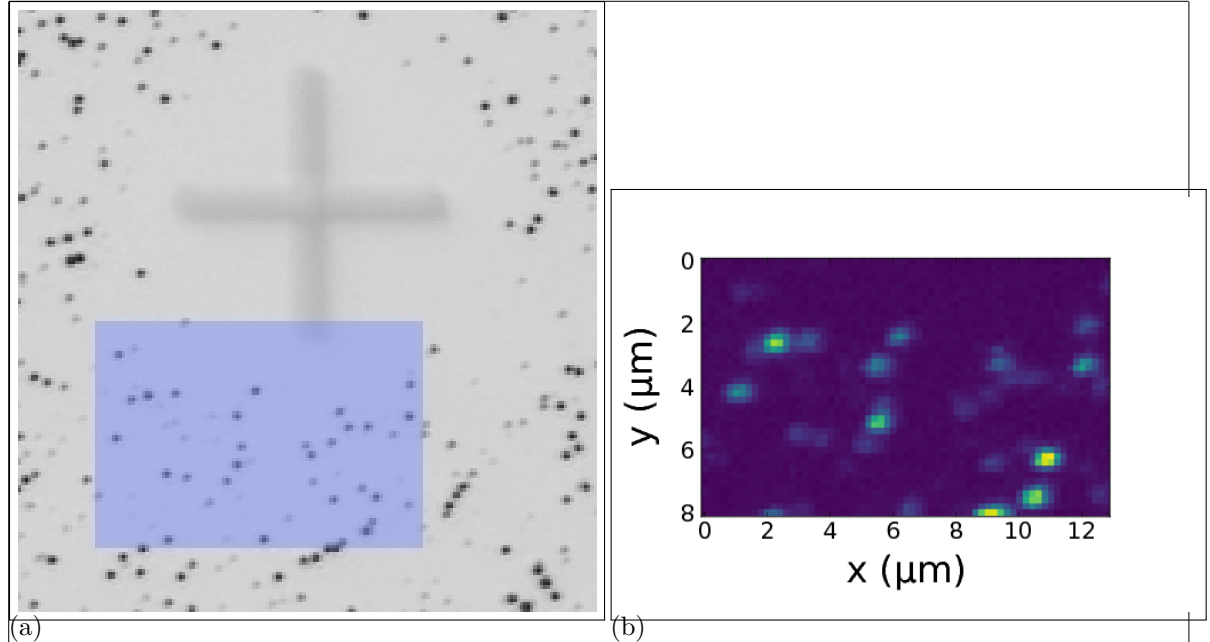


Figure 2.12: (a) Picture recorded with a commercial high resolution laser scanning microscope. The area shaded in blue represents the photoluminescence scan in image (b). (b) Photoluminescence scan of a $8 \mu\text{m} \times 13 \mu\text{m}$

transmittance minimum depends on the film's thickness [60]. Hence the goal is to apply a gold film which suppresses the laser sideband in the SiV center emission regime. In this chapter we showed successful transfer of a nanodiamond containing an SiV center. While the SiV center spectrum was modified after the pick-and-place process, it was clearly identified with the preselected SiV center. Further research has to be performed to enhance the VCSEL emission properties.

2.3 Coupling Nanodiamonds to Double Bowtie Antenna Structures

In this chapter, the integration of SiV centers in nanodiamonds with double bowtie nanoantenna structures is presented. The emission from the coupled system has two advantages:

- The antenna causes an enhancement in the SiV center's photoluminescence emission intensity.
- The photoluminescence spectrum of the nanodiamond is modified depending on the geometry of the nanoantenna as well as the position of the emitter in the gap. This provides the flexibility of designing the nanoantennas to accurately predict and tune the emitters' PL spectrum as desired.

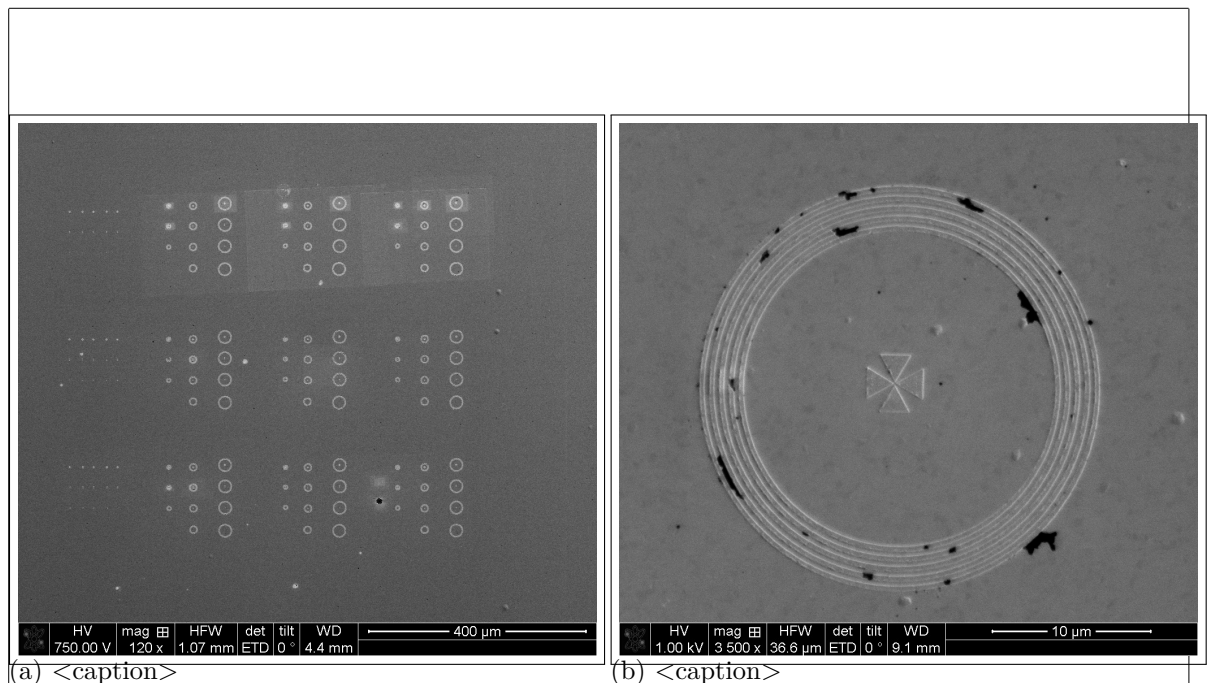


Figure 2.13: <caption>

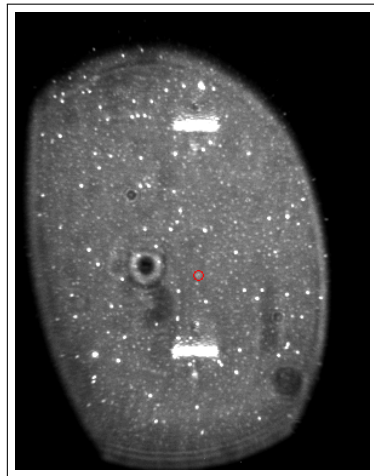


Figure 2.14: Image of the sample surface of 100 nm wet-milled nanodiamonds spin-coated on an iridium substrate illuminated with diffuse white light. The white bars are the horizontal bars of the cross markers which serve as a coarse orientation on the sample surface, the white dots are nanodiamonds, the big black spot is an artifact.

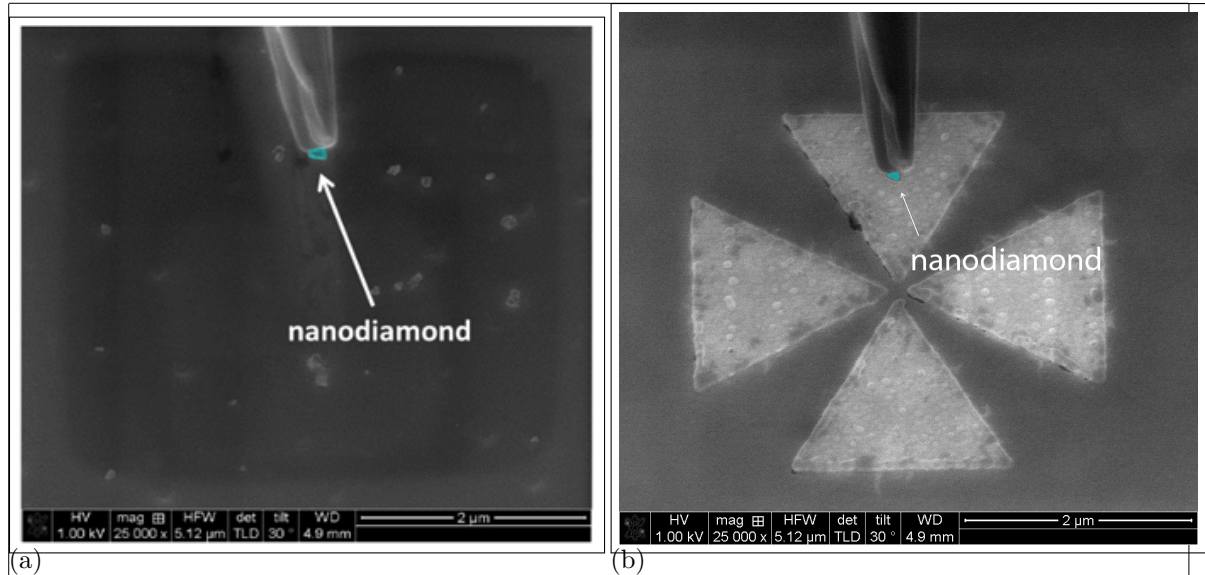


Figure 2.15

2.3.1 Plasmonic Antennas

[61] Optical antennas, acting as converters between propagating and localized fields, provide an effective route to couple photons in and out of nanoscale objects. These antennas are the counterparts of conventional radio and microwave antennas and operate in the visible regime (1, 2). Optical antennas have been shown to focus optical fields to subdiffraction-limited volumes (3), enhance the excitation and emission of quantum emitters (4 \AA), and modify their spectra (8).

A characteristic of antennas is their directed emission and reception. So far, the control of directionality has mainly been pursued by photonic crystal structures (9) and surface-plasmon-based devices (10–12). However, for such structures approaching the nanometer scale diffraction can limit the collimated beaming of light. On the other hand, the interaction of quantum emitters with light is best enhanced with microcavities (13, 14). Compared with these approaches, plasmonic nanoantennas offer a much smaller footprint in an open geometry combining strong subwavelength fields and increased transition rates, together with the prospect of directionality.

[62] from gold, a metal that can develop charge oscillations in its surface layers when excited by optical radiation. These antennas allow visible radiation, which has wavelengths of hundreds of nanometers, to couple into a semiconductor quantum dot only a few nanometers in diameter, and also direct the emission

Good mode-matched antennas reradiate their energy after excitation within a single cycle of the wave. Molecules or quantum dots take nanoseconds or even longer to reradiate their energy. This time scale corresponds to about 1 million oscillations at optical frequencies, and the emission is in all directions.

If an atom, molecule, or quantum dot is placed into the near-field of a metallic nanoantenna (within about 1/50th the wavelength of the emitted radiation), its excited state can radiate photons very efficiently to free space (see the figure, panel B). The quantum emitters can emit a single photon, which can be exploited in quantum optics. Additionally, the

nanoantenna can redirect radiation into a defined solid angle in space and impose a specific polarization on it.

The demonstration of the Purcell effect, which is the acceleration of the decay of the quantum emitter caused by impedance matching by the antenna to free space, could also enhance the radiative emission over nonradiative losses

[63] The electro-magnetic antenna, originally referred to as an "aerial," is a transducer between electromagnetic waves and electric currents, and generally operates in the radiofrequency regime. In analogy with the electro-magnetic antenna, we define the optical antenna as a device that converts freely propagating optical radiation into localized energy, and vice versa. The spatial extent of a receiver or transducer is commonly much smaller than the wavelength of radiation, λ , and is typically of the order of $\lambda/100$.

Surface plasmon resonances make optical antennas particularly efficient at selected frequencies. A generic antenna problem is illustrated in Fig. 3. It consists of a transmitter and a receiver, both represented by dipoles p . The antenna is introduced to enhance the transmission efficiency from the transmitter to the receiver. This enhancement can be achieved by increasing the total amount of radiation released by the transmitter, for which the antenna efficiency is a useful figure of merit:

$$\eta = \frac{P_{rad}}{P_{loss}} \quad (2.1)$$

where P is the total power dissipated by the antenna, P_{rad} is the radiated power and P_{loss} is the power dissipated through other means, such as by absorption in the antenna. However, the transmission efficiency can also be improved by directing the radiation in the direction of the receiver. The efficiency for this process is represented by the directivity:

$$\eta = D(\hat{\theta}, \hat{\phi}) \quad (2.2)$$

where the angles $\hat{\theta}$ and $\hat{\phi}$ represent the direction of observation and $D(\hat{\theta}, \hat{\phi})$ is the angular power density. The combination of antenna efficiency and directivity is referred to as the antenna gain:

$$G = \eta D(\hat{\theta}, \hat{\phi}) \quad (2.3)$$

By reciprocity, we can interchange the fields and sources in Fig. 3 to give $G = \frac{p_1}{p_2} \frac{E_2}{E_1}$, where E_1 (E_2) is the field of dipole p_1 (p_2) evaluated at the location of p_2 (p_1). A good transmitting antenna is therefore also a good receiving antenna. For a transmitter in the form of a two-state quantum emitter, reciprocity leads to a relationship between the emitter's excitation rate \dot{N}_{exc} and its spontaneous emission rate:

$$\eta = \frac{\dot{N}_{exc}}{\dot{N}_{em}} \quad (2.4)$$

Here, the superscript "0" refers to the absence of the antenna and the subscript "1" indicates the polarization state; that is, the electric field vector points in the direction of the $\hat{\theta}$ unit vector. An equivalent equation holds for polarization in the $\hat{\phi}$ direction. Interestingly, excitation in a direction of high directivity allows the excitation rate to be enhanced more strongly than the radiative rate. Another important antenna parameter is the antenna aperture, which is formally the same as the absorption cross-section sigma. Let us consider a dipole-like receiver with a cross-section σ that is not coupled to an antenna. The unit vector in the direction of the absorption dipole axis is denoted as n_p and the incident field at the location of the receiver is E_0 . Once we couple the receiver to an antenna, the field at the receiver increases to E and the cross-section or antenna aperture becomes

$$\eta = \frac{\sigma}{\sigma_0} \quad (2.5)$$

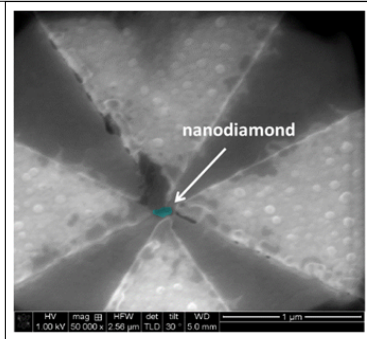


Figure 2.16: <caption>

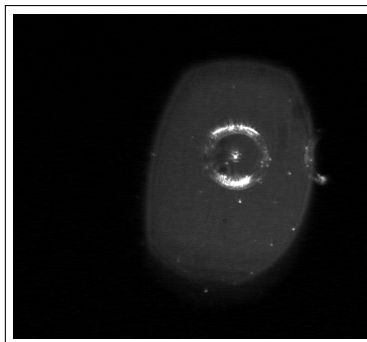


Figure 2.17

Thus, the aperture of an optical antenna scales with the local intensity enhancement factor. Theoretical and experimental studies have shown that intensity enhancements of 10^4 – 10^6 are readily achievable^{14,36,37} and hence, for typical molecules with π -free-space λ ² cross-sections of $\sigma_{\text{mole}} = 1 \text{ nm}^2$, we find that a layer of molecules spaced $0.1\text{--}1 \text{ nm}$ apart can absorb all of the incident radiation if each molecule is coupled to an optical antenna. Of course, this estimate ignores the coupling between antennas and therefore has limited validity.

2.3.2 Structure of the Plasmonic Antennas

FDTD numerical simulations were performed using Lumerical software to characterize gold double bowtie nanoantennas on a gold substrate. The nanoantennas are tailored to have a gap of $g = 150 \text{ nm}$ (taking into account the diameter of the nanodiamonds of around 100 nm), side length of $L = 2 \mu\text{m}$, and a thickness of $t = 60 \text{ nm}$ (see Fig.3a). Upon excitation with incident light, an intense electromagnetic hotspot is formed in the nanoantenna gap [64], which is expected to excite a nanodiamond containing SIV centers aiming to enhance its fluorescence emission. Unlike a single bowtie that is sensitive only to the polarization along its principle axis (C₂ rotational symmetry), a double bowtie features a C₄ rotational symmetry and therefore focuses both parallel and perpendicular polarizations (i.e. all in-plane directions). The index of refraction of gold is taken from Palik [], and that of the nanodiamond is chosen to be $n = 2.4$ at $\lambda = 660 \text{ nm}$. The electric field intensity in the nanoantenna gap is then measured as a function of wavelength to identify the antenna resonance. The spectrum is given in Fig.3b where we observe that the resonance shows two peaks; an intense peak coinciding with the

read paper

Palik, E. D. Handbook of optical constants of solids. 3, (Academic press, 1998)

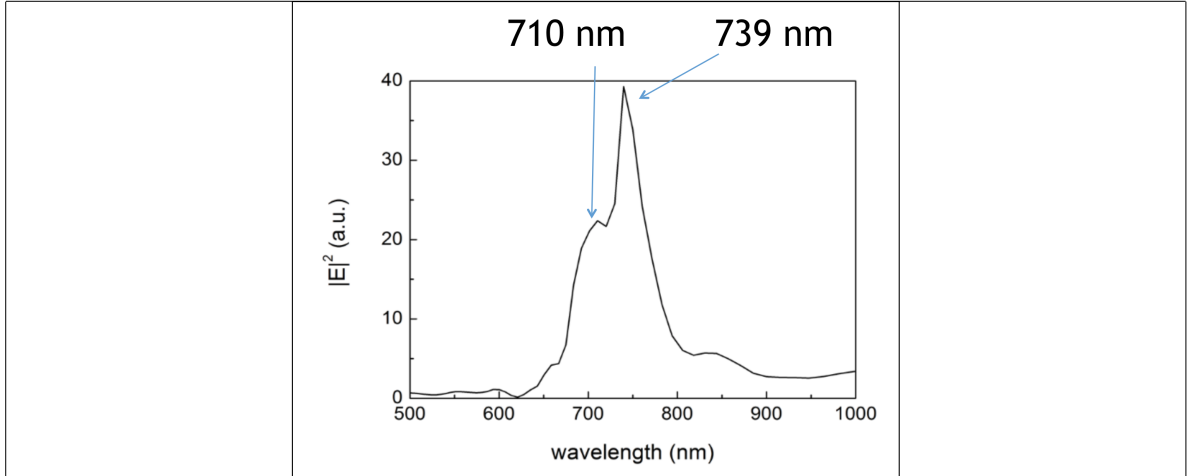


Figure 2.18: <caption>

SiV emission wavelength ($\lambda = 739 \text{ nm}$), and an additional mode at a lower wavelength ($\lambda = 710 \text{ nm}$) [65]. The resonance spectrum of the antenna alone shows only one peak at 739 nm. Thus, the additional peak is attributed to the presence of the nanodiamond that is slightly shifted from the center of the gap, corresponding to our experimental conditions. These calculations suggest, that the emission from an SiV center at 738 nm is effectively enhanced and directed by the antenna.

2.3.3 SiV center in a Plasmonic Antenna

The nanodiamonds exploited for coupling to an antenna were produced by a wet-milling process from a CVD diamond film (A. Muzha, group of A. Krueger, Julius-Maximilians Universität Würzburg, O. Williams, Cardiff University). The solution of nanodiamonds which exhibit a median size of 100 nm were spin-coated on an iridium substrate treated with Piranha etch. To ensure that a pre-characterized nanodiamond exhibiting preferred optical properties (eg. narrow linewidth, high count rate) is later found again, the iridium substrate was engraved with reference cross markers produced by a focused ion beam prior to the spin-coating process. After spin-coating, the sample was placed in an oven for 3 hours at 450 °C to oxidize the surface and remove any residual graphite and amorphous carbon.

Nanodiamond With Multiple SiV centers Coupled to Antenna

Nanodiamond With Single SiV center Coupled to Antenna

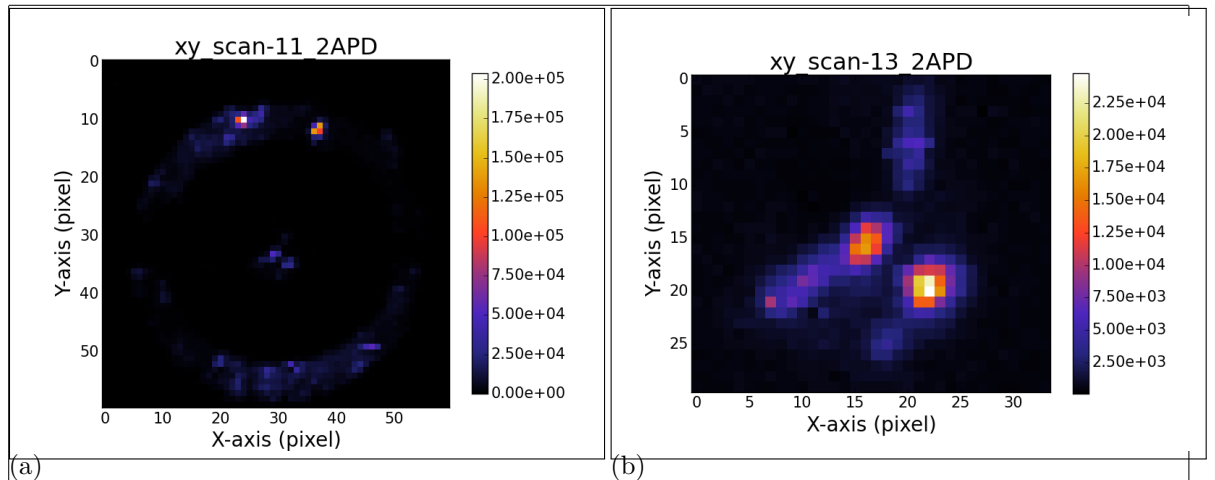


Figure 2.19: <caption>

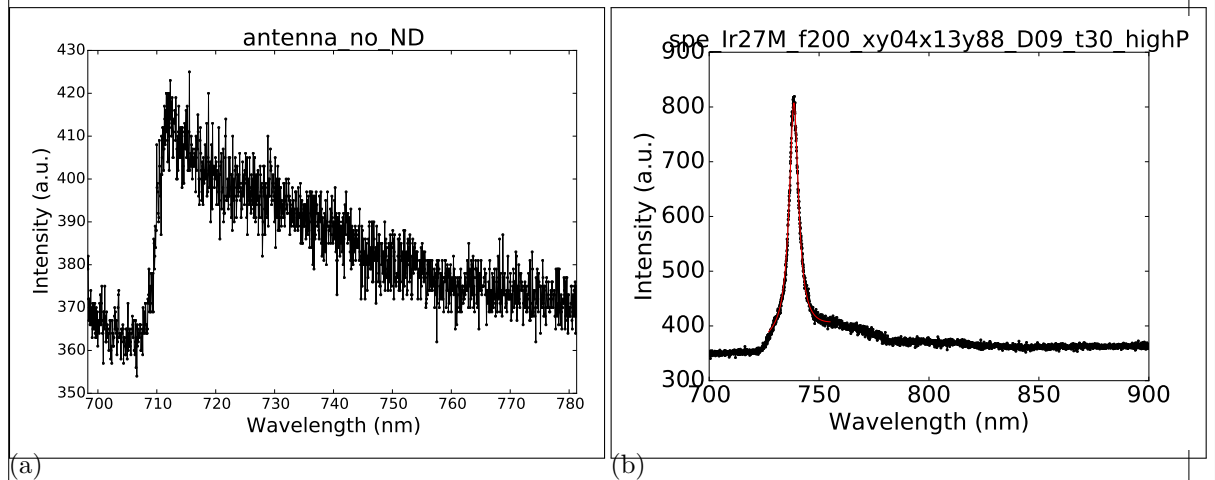


Figure 2.20: <caption>

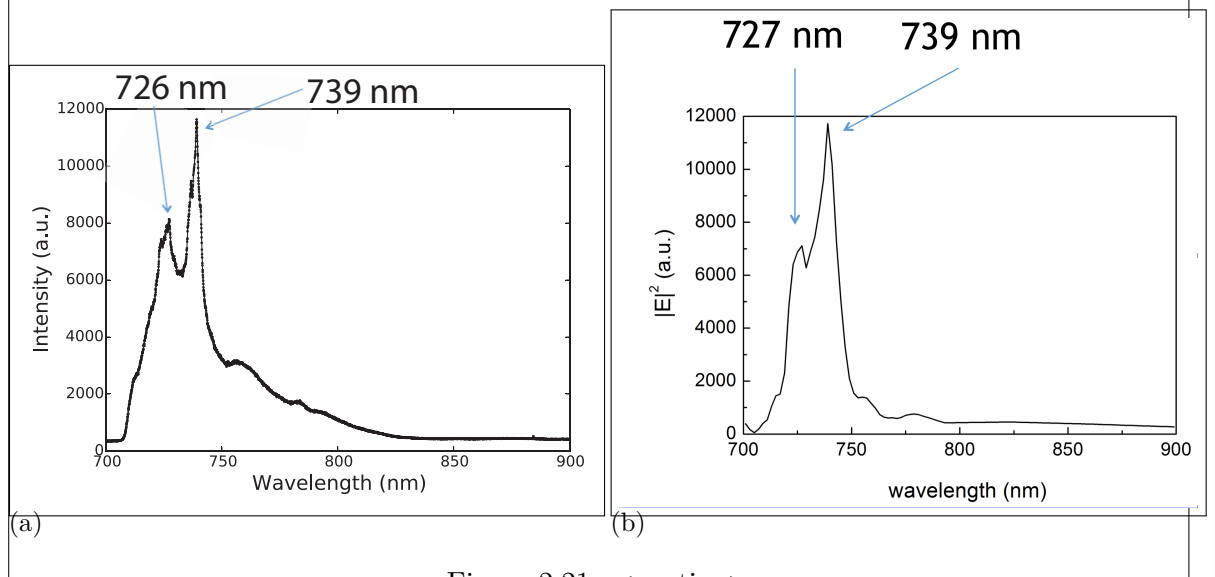


Figure 2.21: <caption>

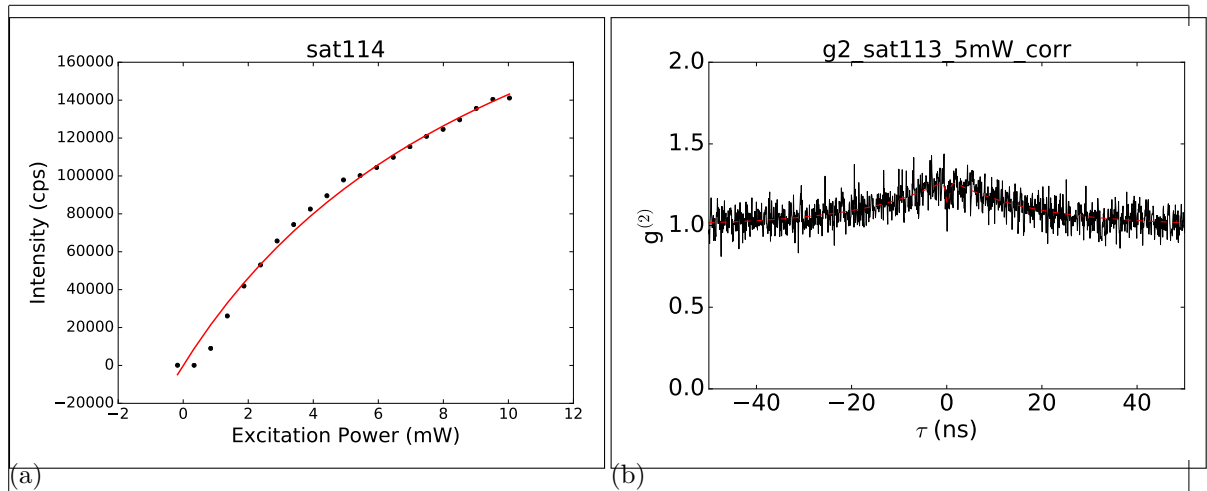


Figure 2.22: <caption>

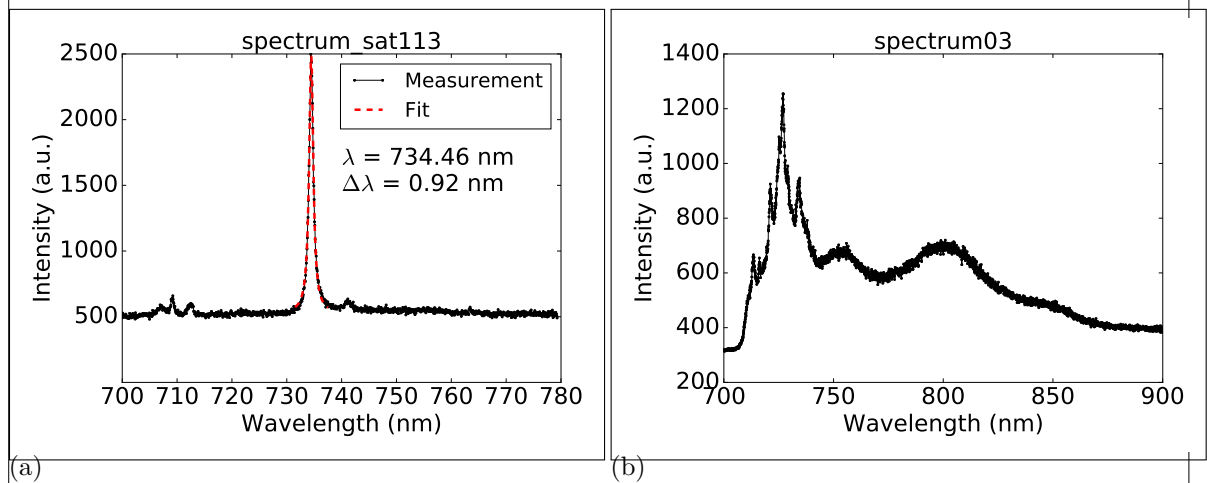


Figure 2.23: <caption>

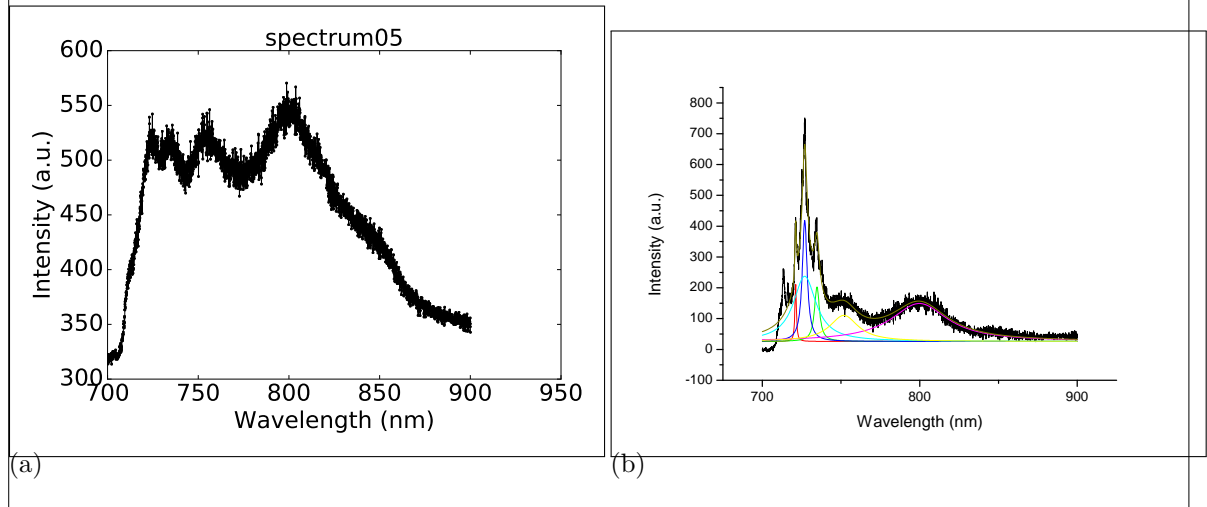


Figure 2.24: <caption>

Bibliography

- [1] Janine Riedrich-Möller, Carsten Arend, Christoph Pauly, Frank Mücklich, Martin Fischer, Stefan Gsell, Matthias Schreck, and Christoph Becher. Deterministic coupling of a single silicon-vacancy color center to a photonic crystal cavity in diamond. *Nano letters*, 14(9):5281–7, aug 2014. 1, 2, 3, 5, 7, 8, 9, 10
- [2] Elke Katja Neu. *Silicon vacancy color centers in chemical vapor deposition diamond : new insights into promising solid state single photon sources*. PhD thesis, 2012. 1, 2, 5, 9
- [3] David Steinmetz. Ni / Si-basierte Farbzentren in Diamant als Einzelphotonenquellen Dissertation. 2011. 1, 4
- [4] F. P. Bundy. Pressure-temperature phase diagram of elemental carbon. *Physica A: Statistical Mechanics and its Applications*, 156(1):169–178, 1989. 1
- [5] Takao Saotome, Kazutoshi Ohashi, Toshimaro Sato, Hiroshi Maeta, Katsuji Haruna, and Fumihisa Ono. Thermal expansion of a boron-doped diamond single crystal at low temperatures. *Journal of Physics: Condensed Matter*, 10(6):1267–1272, feb 1998. 1
- [6] C. D. Clark, P. J. Dean, and P. V. Harris. Intrinsic Edge Absorption in Diamond. *Proceedings of the Royal Society A: Mathematical, Physical and Engineering Sciences*, 277(1370):312–329, feb 1964. 1
- [7] W. Saslow, T. K. Bergstresse, and Marvin L. Cohen. Band structure and optical properties of diamond. *Physical review letters*, 16(9):354–356, 1966. 1
- [8] Richard P. Mildren, James E. Butler, and James R. Rabeau. CVD-diamond external cavity Raman laser at 573 nm. *Optics Express*, 16(23):18950, 2008. 1
- [9] AM Zaitsev. *Optical properties of diamond: a data handbook*. 2001. 2, 3, 4
- [10] Alexios Beveratos, Rosa Brouri, Thierry Gacoin, Jean-Philippe Poizat, and Philippe Grangier. Nonclassical radiation from diamond nanocrystals. *Physical Review A*, 64(6):61802, nov 2001. 2
- [11] W. Kaiser and W. L. Bond. Nitrogen, a major impurity in common type I diamond. *Physical Review*, 115(4):857–863, 1959. 2
- [12] Christopher M. Breeding and James E. Shigley. The "Type" Classification System of Diamonds and Its Importance in Gemology. *Gems & Gemology*, 45(2):96–111, 2009. 2
- [13] John Walker and John Walkert. Optical absorption and luminescence in diamond. *Rep. Prog. Phys.*, 42:1606–1659, 1979. 3

- [14] B. Massarani, J. C. Bourgoin, and R. M. Chrenko. Hopping conduction in semiconducting diamond. *Physical Review B*, 17(4):1758–1769, feb 1978. 3
- [15] M. L. Markham, J. M. Dodson, G. A. Scarsbrook, D. J. Twitchen, G. Balasubramanian, F. Jelezko, and J. Wrachtrup. CVD diamond for spintronics. *Diamond and Related Materials*, 20(2):134–139, 2011. 3
- [16] Gopalakrishnan Balasubramanian, Philipp Neumann, Daniel Twitchen, Matthew Markham, Roman Kolesov, Norikazu Mizuuchi, Junichi Isoya, Jocelyn Achard, Johannes Beck, Julia Tissler, Vincent Jacques, Philip R. Hemmer, Fedor Jelezko, and Jörg Wrachtrup. Ultralong spin coherence time in isotopically engineered diamond. *Nature Materials*, 8(5):383–387, 2009. 3
- [17] P. W. May. Diamond thin films: a 21st-century material. *Philosophical Transactions of the Royal Society A: Mathematical, Physical and Engineering Sciences*, 358(1766):473–495, jan 2000. 3
- [18] Axel Kuhn, Markus Hennrich, and Gerhard Rempe. Deterministic Single-Photon Source for Distributed Quantum Networking. *Physical Review Letters*, 89(6):4–7, 2002. 4
- [19] Matthias Keller, Birgit Lange, Kazuhiro Hayasaka, Wolfgang Lange, and Herbert Walther. Continuous generation of single photons with controlled waveform in an ion-trap cavity system. *Nature*, 431(7012):1075–1078, oct 2004. 4
- [20] P Michler, A Kiraz, C Becher, W V Schoenfeld, P M Petroff, L Zhang, E Hu, and A Imamoglu. A quantum dot single-photon turnstile device. *Science (New York, N.Y.)*, 290(5500):2282–5, dec 2000. 4
- [21] Zhiliang Yuan, Beata E Kardynal, R Mark Stevenson, Andrew J Shields, Charlene J Lobo, Ken Cooper, Neil S Beattie, David A Ritchie, and Michael Pepper. Electrically driven single-photon source. *Science (New York, N.Y.)*, 295(5552):102–5, jan 2002. 4, 8
- [22] Brahim Lounis and Michel Orrit. Single-photon sources. *Reports on Progress in Physics*, 68(5):1129–1179, may 2005. 4
- [23] T. A. Kennedy, J. S. Colton, J. E. Butler, R. C. Linares, and P. J. Doering. Long coherence times at 300 K for nitrogen-vacancy center spins in diamond grown by chemical vapor deposition. *Applied Physics Letters*, 83(20):4190–4192, nov 2003. 4
- [24] Andrew D. Greentree, Barbara A. Fairchild, Faruque M. Hossain, and Steven Prawer. Diamond integrated quantum photonics. *Materials Today*, 11(9):22–31, 2008. 4
- [25] Igor Aharonovich and Elke Neu. Diamond nanophotonics. *Advanced Optical Materials*, 2(10):911–928, 2014. 4
- [26] Steven. Prawer and Igor. Aharonovich. *Quantum information processing with diamond : principles and applications*. Woodhead Publishing, 2014. 4
- [27] N. B. Manson, J. P. Harrison, and M. J. Sellars. Nitrogen-vacancy center in diamond: Model of the electronic structure and associated dynamics. *Physical Review B - Condensed Matter and Materials Physics*, 74(10):1–11, 2006. 4
- [28] F. Jelezko, I. Popa, A. Gruber, C. Tietz, J. Wrachtrup, A. Nizovtsev, and S. Kilin. Single spin states in a defect center resolved by optical spectroscopy. *Applied Physics Letters*, 81(12):2160–2162, 2002. 4

- [29] Charles Santori, David Fattal, Sean M. Spillane, Marco Fiorentino, Raymond G. Beausoleil, Andrew D. Greentree, Paolo Olivero, Martin Draganski, James R. Rabeau, Patrick Reichart, Sergey Rubanov, David N. Jamieson, and Steven Prawer. Coherent population trapping in diamond N-V centers at zero magnetic field. *Conference on Lasers and Electro-Optics and 2006 Quantum Electronics and Laser Science Conference, CLEO/QELS 2006*, 14(17):7986–7994, 2006. 4
- [30] Elke Neu, Mario Agio, and Christoph Becher. Photophysics of single silicon vacancy centers in diamond: implications for single photon emission. *Optics Express*, 20:19956–19971, jul 2012. 4
- [31] A. Sipahigil, K. D. Jahnke, L. J. Rogers, T. Teraji, J. Isoya, A. S. Zibrov, F. Jelezko, and M. D. Lukin. Indistinguishable Photons from Separated Silicon-Vacancy Centers in Diamond. *Physical Review Letters*, 113(11):113602, sep 2014. 4
- [32] Tina Müller, Christian Hepp, Benjamin Pingault, Elke Neu, Stefan Gsell, Matthias Schreck, Hadwig Sternschulte, Doris Steinmüller-Nethl, Christoph Becher, and Mete Atatüre. Optical signatures of silicon-vacancy spins in diamond. *Nature Communications*, 5:3328, feb 2014. 4
- [33] Benjamin Pingault, Jonas N. Becker, Carsten H. H. Schulte, Carsten Arend, Christian Hepp, Tillmann Godde, Alexander I. Tartakovskii, Matthew Markham, Christoph Becher, and Mete Atatüre. All-Optical Formation of Coherent Dark States of Silicon-Vacancy Spins in Diamond. *Physical Review Letters*, 113(26):263601, dec 2014. 4
- [34] Lachlan J. Rogers, Kay D. Jahnke, Mathias H. Metsch, Alp Sipahigil, Jan M. Binder, Tokuyuki Teraji, Hitoshi Sumiya, Junichi Isoya, Mikhail D. Lukin, Philip Hemmer, and Fedor Jelezko. All-optical initialization, readout, and coherent preparation of single silicon-vacancy spins in diamond. *Physical Review Letters*, 113(26):1–5, 2014. 4
- [35] U. F. S. D’Haenens-Johansson, a. M. Edmonds, B. L. Green, M. E. Newton, G. Davies, P. M. Martineau, R. U. a. Khan, and D. J. Twitchen. Optical properties of the neutral silicon split-vacancy center in diamond. *Phys. Rev. B*, 84(24):245208, dec 2011. 5
- [36] J. P. Goss, P. R. Briddon, and M. J. Shaw. Density functional simulations of silicon-containing point defects in diamond. *Physical Review B - Condensed Matter and Materials Physics*, 76(7):1–11, 2007. 5
- [37] Christian Hepp, Tina Müller, Victor Waselowski, Jonas N. Becker, Benjamin Pingault, Hadwig Sternschulte, Doris Steinmüller-Nethl, Adam Gali, Jeronimo R. Maze, Mete Atatüre, Et al., Christoph Becher, Et Al., Christoph Becher, Et Al., Christoph Becher, Et al., Christoph Becher, Et Al., and Christoph Becher. Electronic Structure of the Silicon Vacancy Color Center in Diamond. *Physical Review Letters*, 112(3):036405, jan 2014. 5, 9
- [38] Elke Neu, David Steinmetz, Janine Riedrich-Möller, Stefan Gsell, Martin Fischer, Matthias Schreck, and Christoph Becher. Single photon emission from silicon-vacancy colour centres in chemical vapour deposition nano-diamonds on iridium. *New Journal of Physics*, 13(2):25012, feb 2011. 5
- [39] A T Collins, M F Thomaz, M I B Jorge, A T Collins, A T Collins, A T Collins, P M Spear, A T Collins, A T Collins, M Stanley, A T Collins, S C Lawson, and J Walker. Luminescence decay time of the 1 . 945 eV centre in type. 2177, 1983. 5

- [40] Adam Gali and Jeronimo R. Maze. Ab initio study of the split silicon-vacancy defect in diamond: Electronic structure and related properties. *Physical Review B - Condensed Matter and Materials Physics*, 88(23):1–7, 2013. 5, 6
- [41] K. Iakoubovskii and G.J. Adriaenssens. Optical detection of defect centers in CVD diamond. *Diamond and Related Materials*, 9(7):1349–1356, 2000. 6
- [42] M. C. Rossi, S. Salvatori, F. Galluzzi, R. M. Montereali, and F. Somma. Emission and excitation spectra of silicon-related luminescent centers in CVD-grown diamond films. *Diamond and Related Materials*, 6(10):1564–1567, 1997. 6
- [43] T. Müller, I. Aharonovich, L. Lombez, Y. Alaverdyan, A. N. Vamivakas, S. Castelletto, F. Jelezko, J. Wrachtrup, S. Prawer, and M. Atatüre. Wide-range electrical tunability of single-photon emission from chromium-based colour centres in diamond. *New Journal of Physics*, 13, 2011. 6
- [44] P. Siyushev, V. Jacques, I. Aharonovich, F. Kaiser, T. Müller, L. Lombez, M. Atatüre, S. Castelletto, S. Prawer, F. Jelezko, and J. Wrachtrup. Low-temperature optical characterization of a near-infrared single-photon emitter in nanodiamonds. *New Journal of Physics*, 11, 2009. 6
- [45] G. Davies. The Jahn-Teller effect and vibronic coupling at deep levels in diamond. *Reports on Progress in Physics*, 44(7):787–830, jul 1981. 6, 8
- [46] A. M. Zaitsev. Vibronic spectra of impurity-related optical centers in diamond. *Physical Review B*, 61(19):12909–12922, may 2000. 6, 9
- [47] Marcus W. Doherty, Neil B. Manson, Paul Delaney, Fedor Jelezko, Jörg Wrachtrup, and Lloyd C.L. Hollenberg. The nitrogen-vacancy colour centre in diamond. *Physics Reports*, 528(1):1–45, 2013. 6, 7
- [48] J. L. Dulgall, M. S. Godfrey, K. A. Harrison, W. J. Munro, and J. G. Rarity. Low cost and compact quantum key distribution. *New Journal of Physics*, 8, 2006. 8
- [49] Maximilian Nothaft, Steffen Höhla, Fedor Jelezko, Norbert Fröhlauf, Jens Pflaum, and Jörg Wrachtrup. Electrically driven photon antibunching from a single molecule at room temperature. *Nature Communications*, 3, 2012. 8
- [50] Tom Feng and Bradley D. Schwartz. Characteristics and origin of the 1.681~{eV} luminescence center in chemical-vapor-deposited diamond films. *J. Appl. Phys.*, 73(3):1415, feb 1993. 9
- [51] S. A. Solin and A. K. Ramdas. Raman Spectrum of Diamond. *Physical Review B*, 1(4):1687–1698, feb 1970. 9
- [52] M. H. Grimsditch, E. Anastassakis, and M. Cardona. Effect of uniaxial stress on the zone-center optical phonon of diamond. *Physical Review B*, 18(2):901–904, 1978. 9
- [53] H. Sternschulte, K. Thonke, R. Sauer, P. C. Münzinger, and P. Michler. 1.681-eV luminescence center in chemical-vapor-deposited homoepitaxial diamond films. *Physical Review B*, 50(19):14554–14560, nov 1994. 9
- [54] B. Huttner, N. Imoto, N. Gisin, and T. Mor. Quantum cryptography with coherent states. *Physical Review A*, 51(3):1863–1869, 1995. 9

- [55] C D Clark, H Kanda, I Kiflawi, and G Sittas. Silicon defects in diamond. *Phys. Rev. B*, 51(23):16681–16688, jun 1995. 9
- [56] L J Rogers, K D Jahnke, T Teraji, L Marseglia, C Müller, B Naydenov, H Schauflert, C Kranz, J Isoya, L P McGuinness, and F Jelezko. Multiple intrinsically identical single-photon emitters in the solid state. *Nature communications*, 5:4739, jan 2014. 9
- [57] Andreas Dietrich, Kay D. Jahnke, Jan M. Binder, Tokuyuki Teraji, Junichi Isoya, Lachlan J. Rogers, and Fedor Jelezko. Isotopically varying spectral features of silicon vacancy in diamond. *arXiv preprint arXiv: ...*, 113019:12, 2014. 10
- [58] Aigar Vaigu, Geiland Porrovecchio, Xiao Liu Chu, Sarah Lindner, Marek Smid, Albert Manninen, Christoph Becher, Vahid Sandoghdar, Stephan Götzinger, and Erkki Ikonen. Experimental demonstration of a predictable single photon source with variable photon flux. *Metrologia*, 54(2):218–223, 2017. 11, 15
- [59] Susanne Weidenfeld, Hendrik Niederbracht, Marcus Eichfelder, Michael Jetter, and Peter Michler. Transverse mode and polarization characteristics of AlGaInP-based VCSELs with integrated multiple oxide apertures. In Krassimir Panajotov, Marc Sciamanna, Angel Valle, and Rainer Michalzik, editors, *Proc. SPIE*, volume 8432, page 843205, jun 2012. 16
- [60] A. Axelevitch, B. Gorenstein, and G. Golan. Investigation of Optical Transmission in Thin Metal Films. *Physics Procedia*, 32(April 2016):1–13, 2012. 21
- [61] Alberto G Curto, Giorgio Volpe, Tim H Taminiau, Mark P Kreuzer, Romain Quidant, and Niek F van Hulst. Unidirectional emission of a quantum dot coupled to a nanoantenna. *Science (New York, N.Y.)*, 329(5994):930–933, aug 2010. 23
- [62] Harald Giessen and Markus Lippitz. Physics. Directing light emission from quantum dots. *Science*, 329(5994):910–911, aug 2010. 23
- [63] Lukas Novotny and Niek van Hulst. Antennas for light. *Nature Photonics*, 5(2):83–90, feb 2011. 24
- [64] N. Rahbany, W. Geng, S. Blaize, R. Salas-Montiel, R. Bachelot, and C. Couteau. Integrated plasmonic double bowtie / ring grating structure for enhanced electric field confinement. *Nanospectroscopy*, 1(1):61–66, 2015. 25
- [65] Nancy Rahbany. Towards integrated optics at the nanoscale : plasmon-emitter coupling using plasmonic structures. 2016. 26